Supplement to "The UARS Microwave Limb Sounder version 5 dataset: Theory, characterization and validation"

N.J. Livesey, W.G. Read, L. Froidevaux, J.W. Waters, M.L. Santee,
H.C. Pumphrey[1], D.L. Wu, Z. Shippony[2], and R.F. Jarnot

Jet Propulsion Laboratory, California Institute of Technology, Pasadena

S1. Introduction

For clarity, the section numbering in this supplement is consistent with that of the 'main' part of the paper.

S2. The UARS MLS instrument and operations

No supplementary material.

S3. Theoretical basis

S3.1. Basics of retrieval calculations

The v5 Level 2 data processing algorithms are based on the standard optimal estimation approach [*Rodgers*, 1976, 2000]. The primary aim of the algorithms is to retrieve geophysical profiles of temperature and composition from the input radiance dataset. A state vector $\mathbf{x}$ of length n is constructed that is a representation of aspects of the state of the atmosphere to which the instrument is sensitive. This is typically vertical profiles of temperature and composition, along with some instrumental and other parameters. Section S3.6 describes the MLS state vector for v5. The radiance measurements are represented by a series of vectors $\mathbf{y}_i$, each of length m_i. The retrieval algorithm chooses a value for $\mathbf{x}$ which minimizes the quantity χ^2, defined as

$$\chi^2 = \sum_i [\mathbf{y}_i - \mathbf{f}_i(\mathbf{x})]^{\mathrm{T}} \, \mathbf{S}_{\mathbf{y}_i}^{-1} \, [\mathbf{y}_i - \mathbf{f}_i(\mathbf{x})], \qquad \text{(S1)}$$

where $\mathbf{S}_{\mathbf{y}_i}$ is the error covariance matrix for the measurement vector $\mathbf{y}_i$, and $\mathbf{f}_i$ is the corresponding forward model. The forward model describes the radiances that one would expect to observe from MLS, were the atmosphere in the state represented by $\mathbf{x}$. The Gauss-Newton solution to this minimization can be shown [*Rodgers*, 2000] to be given iteratively by

$$\mathbf{x}^{p+1} = \mathbf{x}^p + \left[\sum_i \mathbf{K}_i^{\mathrm{T}} \mathbf{S}_{\mathbf{y}_i}^{-1} \mathbf{K}_i \right]^{-1} \sum_i \mathbf{K}_i^{\mathrm{T}} \mathbf{S}_{\mathbf{y}_i}^{-1} \left[\mathbf{y}_i - \mathbf{f}_i(\mathbf{x}^p) \right], \qquad \text{(S2)}$$

---

[1]The Institute for Meteorology, University of Edinburgh
[2]Deceased

where the superscript indicates the iterations. $\mathbf{K}_i$ is defined as

$$\mathbf{K}_i = \left. \frac{\partial \mathbf{y}_i}{\partial \mathbf{x}} \right|_{\mathbf{x}=\mathbf{x}^p}, \qquad \text{(S3)}$$

and is commonly known as the matrix of weighting functions or Jacobians. The error covariance matrix for the solution is given by

$$\mathbf{S}_{\mathbf{x}^p} = \left[\sum_i \mathbf{K}_i^{\mathrm{T}} \mathbf{S}_{\mathbf{y}_i}^{-1} \mathbf{K}_i \right]^{-1}. \qquad \text{(S4)}$$

As will be seen later, in the MLS case, most retrieval calculations are sufficiently linear that only one iteration is required.

S3.2. Use of virtual measurements

In most cases, the matrix to be inverted by (S2) is singular. This indicates that there are aspects of the state vector about which the measurement system has been unable to provide any information. This singularity can be avoided by the use of additional measurement vectors containing 'virtual measurements' (as opposed to 'real' measurements such as radiances). In v5, as is typical, these take the form of a priori estimates of some or all elements of the state vector, usually formed from some climatology or model data. We choose to represent these by the vector $\mathbf{a}$ of the same length and physical meaning as $\mathbf{x}$, with associated error covariance $\mathbf{S}_{\mathbf{a}}$. The weighting function matrix associated with $\mathbf{a}$ is simply the $n \times n$ identity matrix. Equation (S2) then becomes:

$$\mathbf{x}^{p+1} = \mathbf{x}^p + \left[\mathbf{S}_{\mathbf{a}}^{-1} + \sum_i \mathbf{K}_i^{\mathrm{T}} \mathbf{S}_{\mathbf{y}_i}^{-1} \mathbf{K}_i \right]^{-1}$$
$$\left(\mathbf{S}_{\mathbf{a}}^{-1} \left[\mathbf{a} - \mathbf{x}^p \right] + \sum_i \mathbf{K}_i^{\mathrm{T}} \mathbf{S}_{\mathbf{y}_i}^{-1} \left[\mathbf{y}_i - \mathbf{f}_i(\mathbf{x}^p) \right] \right), \qquad \text{(S5)}$$

with solution error covariance

$$\mathbf{S}_{\mathbf{x}^p} = \left[\mathbf{S}_{\mathbf{a}}^{-1} + \sum_i \mathbf{K}_i^{\mathrm{T}} \mathbf{S}_{\mathbf{y}_i}^{-1} \mathbf{K}_i \right]^{-1}. \qquad \text{(S6)}$$

and the definition of χ^2 expanding to

$$\chi^2 = [\mathbf{a} - \mathbf{x}]^{\mathrm{T}} \mathbf{S_a}^{-1} [\mathbf{a} - \mathbf{x}]^{\mathrm{T}} +$$
$$\sum_i [\mathbf{y}_i - \mathbf{f}_i(\mathbf{x})]^{\mathrm{T}} \mathbf{S_{y}}_i^{-1} [\mathbf{y}_i - \mathbf{f}_i(\mathbf{x})] . \quad (S7)$$

There is a subtlety in that there can be some elements of $\mathbf{x}$ for which an a priori estimate is not required. For these, the corresponding rows and columns of $\mathbf{S_a}^{-1}$ are set to zero (note that this makes $\mathbf{S_a}^{-1}$ singular and therefore $\mathbf{S_a}$ undefined, though this is not a problem as $\mathbf{S_a}$ is never explicitly required). An example in v5 of such an exception is tangent pressure, as described in section S3.8.

Care must be taken when using data that have been retrieved in conjunction with a priori information. The error covariance of the solution must be compared with that of the a priori. If the solution error covariance is little changed from the a priori error covariance, then this indicates that the radiance measurements have added little information to the state vector, and the result is strongly biased toward the a priori.

The addition of the a priori term changes the χ^2 hypersurface to favor solutions close to the a priori. In addition, it is possible to favor solutions whose deviations from the a priori are correlated (i.e., smoother) by using non-zero values for the off-diagonal terms in the a priori covariance matrix. In v5, sections of the a priori covariance matrix describing particular parameters (e.g., temperature and composition profiles) are filled according to

$$[\mathbf{S_a}]_{ij} = \sqrt{[\mathbf{S_a}]_{ii} [\mathbf{S_a}]_{jj}} \exp\left[-\frac{|z_i - z_j|}{l} \right], \quad (S8)$$

where z_i, z_j are the height of surfaces i and j and l is some characteristic correlation length scale, all in log pressure coordinates (see section S3.6 for a discussion of the MLS vertical coordinate system). An exponential form is used, corresponding to the covariance that would be obtained from a Markov process (i.e., random walk). Forms such as Gaussian that are 'broader' are numerically unstable, as the resulting covariance matrix is close to being positive indefinite, except for small (i.e., not particularly effective) values of l.

S3.3. Constrained quantity error propagation

For efficiency and simplicity, retrieval algorithms are often implemented in a series of phases. For example, in v5, for the data taken up to April 1993, the first phase is a retrieval of temperature and tangent pressure taken from the observations of molecular oxygen emission (band 1). This is followed by a retrieval of stratospheric ozone and water

vapor (bands 5 and 6). The previously-obtained temperature and pressure values are used as constrained parameters in the forward model for these later retrievals. However, the knowledge of these 'constrained quantities' is imperfect; their error covariance has been estimated in the earlier phase by (S6). This uncertainty is accounted for in the later retrievals by adding an additional term to the error covariance of the radiances used in these later phases, according to:

$$\mathbf{S_{y}}_i \rightarrow \mathbf{S_{y}}_i + \left(\mathbf{K}_i^c\right) \mathbf{S}^c \left(\mathbf{K}_i^c\right)^{\mathrm{T}}, \quad (S9)$$

where $\mathbf{K}_i^c$ is the matrix of weighting functions for $\mathbf{y}_i$ describing the sensitivity of the radiances to be used in the later phase (e.g., emission from ozone and water vapor) to the constrained quantities (e.g., temperature and pressure), and $\mathbf{S}^c$ is the error covariance of the constrained quantities estimated by (S6) in the earlier phase.

The original $\mathbf{S_{y}}_i$ matrices for MLS, are diagonal, as there is no significant correlation in radiance noise between channels or integration periods. This makes the inversion of $\mathbf{S_{y}}_i$ in (S5) computationally simple. However, including the uncertainty in the constrained quantities in the error budget makes the updated $\mathbf{S_{y}}_i$ matrices non-diagonal. Their inversion becomes the most computationally intensive aspect of the calculation, due to the large number of measurements compared to state vector elements.

Approximations such as ignoring the off-diagonal terms in the new $\mathbf{S}_i$ matrices are undesirable, as they correspond to a loss of information, tying the retrieval closer to the a priori information. The approach taken in v5 was to partition the problem to achieve an acceptable compromise between speed and accuracy. The metric used to assess the accuracy was a comparison of the estimated precision reported by the retrieval with the observed scatter in the retrieved species in regions where atmospheric variability is expected to be low (e.g., the tropical stratosphere for some species). For selected bands, the full non-diagonal error propagation calculation was performed on all the radiances whose tangent points were at pressures greater than a given threshold (22 hPa), with simple diagonal propagation used at smaller pressures. Radiance observations above and below this threshold tangent pressure were divided into separate measurement vectors (Equation (S2)), and the corresponding $\mathbf{K}_i^{\mathrm{T}} \mathbf{S_{y}}_i^{-1} \mathbf{K}_i$ calculation was performed using either the full $\mathbf{S_{y}}_i$ matrix or its diagonal. This compromise was seen to give generally good comparisons between estimated precision and observed scatter for all species, while not involving too much computational effort. Section S4 gives details of the specific implementation of this calculation in v5.

S3.4. Diagnosing retrieval performance

A very important diagnostic of retrieval performance is the estimated precision. As explained in section S3.2, this should be compared with the precision placed on the a priori estimates of the state vector components. As an aid to users of MLS data, the sign of the precision in the data files is set negative if it is no better than 50% of the a priori precision. This indicates that at least 25% of the information in the result has come from the a priori, and therefore the data should probably not be used.

Another diagnostic of retrieval performance is the χ^2 statistic given in (S1). Large values of χ^2 may indicate instrument anomalies, or deficient instrument calibration, spectroscopy information, or inaccurate forward models. They can also indicate atmospheric states far from the a priori state estimate. In v5, contributions to χ^2 from the radiances are summarized by a set of flags that indicate which profiles can be considered reliable. These flags are discussed in section 5.

Another useful measure of retrieval performance is the matrix of averaging kernels (**A**) [*Rodgers*, 1990], given by

$$\mathbf{A} = \frac{\partial \hat{\mathbf{x}}}{\partial \mathbf{x}_t} = \left[\mathbf{S_a}^{-1} + \sum_i \mathbf{K}_i^{\mathrm{T}} \mathbf{S}_{\mathbf{y}_i}^{-1} \mathbf{K}_i \right]^{-1} \sum_i \mathbf{K}_i^{\mathrm{T}} \mathbf{S}_{\mathbf{y}_i}^{-1} \mathbf{K}_i,$$
(S10)

where **x** is the state vector obtained from the retrieval and $\mathbf{x}_t$ describes the unknown true state of the atmosphere. The columns of **A** describe the response of the retrieval system to delta function perturbations in the atmosphere. The rows of **A** indicate which parts of the atmosphere have contributed to each retrieval level. The widths of the peaks seen in these rows are a useful measure of the vertical resolution of the retrieved dataset. In the ideal case **A** would be the identity matrix.

S3.5. The Marquardt-Levenberg approach

Some of the retrieval calculations are sufficiently nonlinear that the Marquardt-Levenberg algorithm is more appropriate than the standard Gauss-Newton method. This formulates the retrieval as:

$$\mathbf{x}^{p+1} = \mathbf{x}^p + \left[\gamma \mathbf{I}_n + \mathbf{S_a}^{-1} + \sum_i \mathbf{K}_i^{\mathrm{T}} \mathbf{S}_{\mathbf{y}_i}^{-1} \mathbf{K}_i \right]^{-1} \left(\mathbf{S_a}^{-1} [\mathbf{x} - \mathbf{a}] + \sum_i \mathbf{K}_i^{\mathrm{T}} \mathbf{S}_{\mathbf{y}_i}^{-1} [\mathbf{y}_i - \mathbf{f}_i(\mathbf{x}^p)] \right),$$
(S11)

where $\mathbf{I}_n$ is the $n \times n$ identity matrix, and γ is a scalar. As γ is reduced, this iteration tends toward the Gauss-Newton

iteration of (S5). Conversely, as γ is increased, this iteration tends toward the more cautious steepest descent algorithm with a step size proportional to γ^{-1}. In v5 the Marquardt-Levenberg algorithm is implemented by first setting γ to some fairly large value that is then increased or decreased by some factor each iteration, according to the change seen in χ^2. If χ^2 decreases, then the value of γ is decreased, making the next iteration more aggressive. If, conversely, χ^2 increases, then the result of the iteration is rejected, and a new iteration is attempted using a larger value of γ.

S3.6. Construction of the MLS state vector

The most important components of the state vector for v5 are vertical profiles of temperature and species abundances fit to a set of fixed pressure levels. The geopotential height of the 100 hPa pressure surface is also a state vector element (storing a vertical profile of geopotential height is inappropriate, as the information it would convey is already present in the temperature profile when hydrostatic balance, implicit in all the forward model calculations, is imposed). The geopotential height at 100 hPa is chosen as a priori data is readily available for this region. It is used in the retrieval calculations only as a constant in an integration, so the choice of pressure has no direct impact on the quality of the geopotential height observations.

In the case of temperature and composition, the terms in the state vector describe the tie points in a piecewise linear representation of the vertical profile (temperature or volume mixing ratio). An exception to this is water vapor, for which the representation basis below 100 hPa represents a piecewise linear interpolation in log mixing ratio. This is a better model of the vertical structure of water vapor profiles in this region, which display quasi-exponential growth with increasing pressure, and is equivalent to a linear interpolation in relative humidity with respect to ice. All the forward model calculations accurately model these representations (rather than using, for example, a layer mean).

The task of the retrieval algorithm is to deduce an optimum value of the state vector consistent with the observed radiances, tangent point altitudes, and a priori information. The forward model calculations that form part of the algorithm need some additional parameters in order to match these observations. The most important of these are the limb tangent point pressures (or more precisely $-\log_{10} [\text{tangent pressure} / \text{hPa}]$, as this is a less non-linear variable) for each minor frame. The tangent point pressures for the 63-GHz observations are retrieved from the molecular oxygen signal in the 63-GHz radiances. The tangent pressures for the other radiometers are deduced from the 63-GHz tangent pressures, using estimates of the angular offsets of the radiometer fields of view taken from ground- and

space-based calibration. These angular offsets are part of the state vector (although not retrieved).

Some atmospheric constituents (e.g., nitrous oxide, ozone isotopes, etc.) contribute to the MLS radiances in a manner too insignificant to yield useful MLS observations of their abundance, but not so insignificant that their effects can be neglected. The abundances of these constituents are also included in the state vector, and constrained to climatological values (section S4 describes this in more detail).

Our use of the term 'state vector' is different from that adopted in, for example, *Rodgers* [1976]. We use the term state vector to describe all the variable (or potentially variable) parameters needed by the forward model, whether they are retrieved or not.

Most of the MLS data products are based upon measurements of spectral contrast (channel to channel variations in the observed radiances). The instrument resolves a spectral line, or a set of lines, and the spectral form of the signal yields information on the state vector. The observed spectral lines are superimposed on some spectrally flat offset, which arises through both instrumental effects such as thermal emission from the antenna, and atmospheric effects such as continuum emission.

The offset is modeled in the retrieval as a scan independent absolute radiance offset, plus a vertical profile of extinction coefficient on the same pressure surfaces as used for the atmospheric constituents. The former is intended to capture the instrumental effects, which are typically independent of scan angle; the latter is a good model of unexplained atmospheric absorption (e.g., due to unexplained or unmodelled absorption such as continuum from far wings of lines). In order to partition these appropriately, the extinction coefficient is not retrieved for pressures less than $0.068\,\mathrm{hPa}$. There are two exceptions to this scheme. The first is the case of the retrieval of temperature, tangent pressure and geopotential height from the 63-GHz radiances. Here, an independent radiance baseline offset is retrieved for each tangent height, as this was found to better model the residual radiances seen in this band. The second exception is the UTH retrieval, which is based on observations from one channel as opposed to spectral contrast, so baseline or extinction retrievals are not appropriate. This retrieval inherently assumes that instrument effects, air continuum and contamination from other species is either sufficiently well understood or negligible that we do not need to retrieve additional baseline-type components like extinction.

S3.7. The MLS Suite of Forward Models

For the majority of the MLS channels, the forward model used in v5 is based on a linear approximation (see sec-

tion S3.7.6). The coefficients used in this approximation are taken from the results of a 'full' forward model. The 'full' model is also used directly in v5 for appreciably nonlinear radiances used for the upper tropospheric humidity (UTH) retrieval and for some channels in the retrieval of the 183-GHz H_2O and O_3.

The full forward model is given by

$$
\begin{aligned}
\hat{I}_{\mathrm{ch}}^{\mathrm{L}} = r_u &\frac{\int_{\Omega_A} \int_{\nu_{\mathrm{lo}}}^{\infty} I\left(\nu, \Omega, \mathbf{x}\right) \Phi\left(\nu\right) G\left(\Omega, \Omega_t, \nu\right) \mathrm{d}\Omega \mathrm{d}\nu}{\int_{\Omega_A} \int_{\nu_{\mathrm{lo}}}^{\infty} \Phi\left(\nu\right) G\left(\Omega, \Omega_t, \nu\right) \mathrm{d}\Omega \mathrm{d}\nu} \\
+ r_l &\frac{\int_{\Omega_A} \int_{-\infty}^{\nu_{\mathrm{lo}}} I\left(\nu, \Omega, \mathbf{x}\right) \Phi\left(\nu\right) G\left(\Omega, \Omega_t, \nu\right) \mathrm{d}\Omega \mathrm{d}\nu}{\int_{\Omega_A} \int_{-\infty}^{\nu_{\mathrm{lo}}} \Phi\left(\nu\right) G\left(\Omega, \Omega_t, \nu\right) \mathrm{d}\Omega \mathrm{d}\nu},
\end{aligned}
\tag{S12}
$$

where $\hat{I}_{\mathrm{ch}}^{\mathrm{L}}$ is the measured calibrated radiance for channel ch, ν_{lo} is the local oscillator frequency, r_u is the higher frequency (relative to ν_{lo}) sideband relative response for channel, ch, r_l is the lower frequency sideband relative response for channel, ch ($r_l + r_u \equiv 1$). $I\left(\nu, \Omega, \mathbf{x}\right)$ is the atmospheric limb radiance, $\Phi\left(\nu\right)$ is the instrument spectral response for channel ch, $G\left(\Omega, \Omega_t, \nu\right)$ is the antenna field of view (FOV) response function, ν is frequency, Ω is solid angle, Ω_t is the FOV boresight direction, Ω_A is the integration limit in solid angle, and $\mathbf{x}$ is the forward model state vector. The state vector contains coefficients for evaluating a vertical profile of the constituent concentrations (f) and temperature (T), negative base 10 logarithm of the FOV direction limb tangent pressure (ζ_t), and some geometric and hydrostatic quantities for converting tangent pressure into pointing angles and heights. Embedded in the forward model is hydrostatic equilibrium, which relates height to pressure and temperature.

Note that by taking r_u and r_l outside the frequency integral, we have neglected their possible small variations over the width of an individual filter channel. Also note that we have neglected the small variations in field of view response over the filter width by separating G and Φ. This approximation is further extended by using the same $G\left(\Omega, \Omega_t, \nu\right)$ for all channels in a radiometer. The FOV width across a radiometer changes by less than 1% across all its channels which is smaller than the measured FOV beam width uncertainty of 5% [*Jarnot et al.*, 1996]. A 5% beam width error is shown to have negligible impact upon the 205 and 183 GHz ozone retrievals [*Froidevaux et al.*, 1996], which will hold for all retrieved species.

The next four sub-subsections describe the components of this calculation, starting with the field of view integration and finishing with the computation of $I\left(\nu, \Omega, \mathbf{x}\right)$. The fifth sub-subsection describes the forward model derivative algorithm.

S3.7.1. Field of view integration The FOV integration assumes there is no frequency variation in the antenna gain function G inside a band, which makes the spectral and spatial integrations separable. The limb radiance is assumed to have negligible variability across the <24 km azimuth (horizontal) width of the FOV, allowing the FOV shape to be collapsed into a one dimensional function in elevation (vertical) angle, χ ($G[\Omega, \Omega_t, \nu] \rightarrow G[\chi, \chi_t, \nu]$). As the FOV function in χ is the same at all pointing positions, χ_t, the spatial integral can be converted into a convolution integral, and solved with fast Fourier transforms. This gives

$$\hat{I}_{ch}^{L}(\chi_t, \mathbf{x}) = \mathcal{F}^{-1} \left\{ \mathcal{F}\left[\overline{I}_{ch}^{L}(\chi, \mathbf{x})\right] \mathcal{F}[G(\chi_t - \chi)]\right\}, \tag{S13}$$

where $\overline{I}_{ch}^{L}$ is the spectrally integrated limb radiance for channel ch, $\mathcal{F}$, and $\mathcal{F}^{-1}$ are the Fourier transform operator and its inverse respectively. Elevation angles χ and χ_t are computed by

$$\chi = \sin^{-1}\left[\frac{(1+n)\,h_c \min(h_c, h_\oplus)}{h_s h_\oplus}\right], \tag{S14}$$

where h_c is the unrefracted tangent geocentric altitude for elevation angle χ, $1 + n$ is the refractive index at h_c, $h_\oplus$ is the geocentric Earth radius, and h_s is the geocentric satellite altitude. The refractive index minus one, n, is given by

$$n = \frac{7.76 \times 10^{-5} P}{T}\left[1 + 4810\frac{f^{H_2O}}{T}\right], \tag{S15}$$

where $P(=10^{-\xi_t})$ is tangent pressure in hPa, T is tangent temperature in Kelvins, and f^{H_2O} is the tangent water vapor volume mixing ratio. The sine of the incident line of sight (LOS) angle perpendicular to the tangent surface is $\min(h_c, h_\oplus)/h_\oplus$, which is unity except for Earth intersecting rays. Geocentric altitude, h_c, is computed from the hydrostatic equation, which depends on the temperature profile, tangent pressure, and a reference height. Its calculation is based on those described in section S3.8. A cubic spline computation [*de Boor*, 1987] interpolates the computed radiances to a grid of 1024 equally-spaced points (covering ± 0.1 radians) in the convolution. There will be a small contribution due to signals impinging on the antenna at absolute angles greater than 0.1 radians which is estimated and removed from the calibrated radiances produced by level 1 processing.

S3.7.2. Spectral integration The spectral integration is

$$\overline{I}_{ch}^{L}(\chi, \mathbf{x}) = r_u \frac{\int_{\nu_{lo}}^{\infty} I(\nu, \mathbf{x})\,\Phi(\nu)\,d\nu}{\int_{\nu_{lo}}^{\infty} \Phi(\nu)\,d\nu}$$
$$+ r_l \frac{\int_{-\infty}^{\nu_{lo}} I(\nu, \mathbf{x})\,\Phi(\nu)\,d\nu}{\int_{-\infty}^{\nu_{lo}} \Phi(\nu)\,d\nu} \tag{S16}$$

where $I(\nu, \mathbf{x}) \equiv I(\nu, \Omega, \mathbf{x})$ but with $\Omega \rightarrow \chi$ dependence dropped because it is dependent on $h_\oplus$ and h_s, which are state vector elements, and h_c and n which are functions of the state vector quantities tangent pressure, temperature, water vapor, and reference geopotential height. The spectral integration uses a 161 point trapezoidal quadrature, based on the measured channel filter shape, $\Phi(\nu)$. The radiative transfer calculation is evaluated on far fewer points and interpolated to the frequencies represented by the 161 points. The spectral characteristics of the radiance signal within the channel determines the method and the frequency gridding used by the radiative transfer calculations. In some cases a 'pre-frequency-averaging' approximation can be made. With this, only one radiance calculation per channel is performed, using a precomputed filter-shape-weighted average absorption coefficient derivative with respect to mixing ratio (cross section). This can be implemented in cases where radiances are optically thin (total single sideband radiances less than 100 K), such as ozone in band 4, or in any band having very little spectral variation irrespective of absolute radiance, such as bands 2 and 3.

Bands 1, 5, and 6 have optically thick signals with large spectral variation. The signals from these are calculated with a filter-weighted average of radiance calculations. If there is only one spectral line in a channel, the radiances are computed on a 25 point equally-spaced frequency grid within the channel, and an Aitkin's Δ^2 method is used [*Isaacson and Keller*, 1994]. The filter weighted integral is evaluated three times using radiance calculations at 7, 13 and finally all 25 frequencies. Each time the radiances are interpolated with cubic splines to the 161 point filter shape frequency grid and evaluated with a trapezoid quadrature. The results form a three term series converging to a better solution. This approach is used for center channels in band 1 and all the channels in bands 5 and 6.

Aitkin's method does not work well in cases where there are multiple spectral lines within the channel (e.g., the ^{18}OO and ^{17}OO lines in the wing channels of band 1). In these cases an adaptive computation is implemented. The adaptive computation starts by evaluating the radiative transfer on $2n+1$ frequency points, where n is the number of lines in the channel. The initial frequency grid consists of points at the channel boundaries, line centers, and midway between lines.

This defines $2n$ integration regions. In each region, two integrals are evaluated: one using only the two end points, the other also including a point at the center of the region. If the difference between these is below a specified threshold, the integration between these points has adequately converged and the calculation proceeds to the next unconverged region, otherwise the region is split at the center and the process starts again. When all regions between the channel boundaries are converged, the calculation is complete.

S3.7.3. Radiative transfer calculation The MLS limb radiance, $I(\nu, \mathbf{x})$, is modeled with a nonpolarized, nonscattering, radiative transfer calculation for atmospheric emitters in local thermodynamic equilibrium. The integration, along the LOS path, beginning at the instrument ($s = 0$), passing through the atmosphere ($s > 0$) and out into space ($s \rightarrow \infty$), is given by

$$
\begin{aligned}
I(\nu, \mathbf{x}) = & \, I_o(\nu) \, \Upsilon \tau(t, \infty, \nu, \mathbf{x}) \, \tau(0, t, \nu, \mathbf{x}) \\
& + B[\nu, T(t, \mathbf{x})](1 - \Upsilon) \, \tau(0, t, \nu, \mathbf{x}) \\
& + \Upsilon \tau(0, t, \nu, \mathbf{x}) \int_{s=\infty}^{s=t} B[\nu, T(s, \mathbf{x})] \alpha(\nu, \mathbf{x}, s) \, \tau(t, s, \nu, \mathbf{x}) \, \mathrm{d}s \\
& + \int_{s=t}^{s=0} B[\nu, T(s, \mathbf{x})] \alpha(\nu, \mathbf{x}, s) \, \tau(0, s, \nu, \mathbf{x}) \, \mathrm{d}s, \quad \text{(S17)}
\end{aligned}
$$

where $B[\nu, T(s, \mathbf{x})]$ is the Planck blackbody function, $T(s, \mathbf{x})$ is the temperature, which is a part of state vector $\mathbf{x}$, I_o is the cosmic space radiance, $\tau(a, b, \nu, \mathbf{x})$ is the transmission function between points a and b along s, Υ is the Earth surface reflection coefficient, t is the tangent point on s, and $\alpha(\nu, \mathbf{x}, s)$ is the absorption coefficient. The transmission function is given by

$$
\tau(a, b, \nu, \mathbf{x}) = \exp\left[-\int_{s'=a}^{s'=b} \alpha(\nu, \mathbf{x}, s') \, \mathrm{d}s'\right], \quad \text{(S18)}
$$

where a and b are the integration limits and s' is path length. The Earth reflection coefficient, Υ is 1 for non Earth intersecting rays and 0.05 (microwave reflectivity for land) for Earth intersecting rays. The opacity of the MLS limb is sufficiently high that the Earth is rarely observed (the only exception is occasionally near the south pole in winter) and therefore is not sensitive to the Υ value. It is included merely to correctly treat the Earth intersecting ray case. The limb viewing geometry used by MLS makes the measurements insensitive to Υ for the LOS Earth intersecting paths, and therefore a model that considers surface reflectivity variations is not needed. Equation (S17) is solved piece-wise by a summation over layers, using the discrete differential temperature radiative transfer equation [*Read et al.*, 1995],

$$
\begin{aligned}
I(\nu, \mathbf{x}) \approx I_t = & \sum_{i=t}^{N} \Delta B_i \prod_{k=i}^{N-1} \Delta \tau_{kt} \\
& - \Upsilon \left(\prod_{k=t}^{N-1} \Delta \tau_{kt}\right) \times \left[\sum_{i=t}^{N} \Delta B_i \prod_{k=t}^{i-1} \Delta \tau_{kt}\right. \\
& \left. - I_o \left(\prod_{k=t}^{N-1} \Delta \tau_{kt}\right)\right]. \quad \text{(S19)}
\end{aligned}
$$

Equation (S19) is applied to an $N - 1$ layered atmosphere where each layer is separated by surfaces with indices running from 1 (the Earth surface) to N (top of the $N-1$ layer).

Radiances are computed for a set of LOS tangents that are a subset (indices t) of the N surfaces (interpolation to the required tangents is performed later). Subscripts i and k indicate the surfaces used in the products and sums. The quantities ΔB_i are $(B_{i-1} - B_{i+1})/2$, except when $i = N$, where ΔB_N is $(B_{N+1} + B_N)/2$. The Planck blackbody function B_i is divided by Boltzmann's constant to yield radiances in units of Kelvins, as reported in the MLS Level 1 data [*Jarnot et al.*, 1996]. The four product terms are the atmospheric LOS transmissions from (1) layer i to the instrument, (2) tangent layer t to the instrument, (3) layer i to the tangent layer t, and (4) from space to layer t. Any product for a term which does not exist (e.g., when $i = N$ in the first term and $i = t$ in the third term), is set to unity. The layer transmission $\Delta \tau_{kt}$ is given by

$$
\Delta \tau_{kt} = \exp\left[-\frac{\Delta s_{k \to k+1}^{\mathrm{refr}}}{\Delta s_{k \to k+1}} \int_{\zeta_k}^{\zeta_{k+1}} \alpha(\nu, \mathbf{x}, \zeta) \frac{\mathrm{d}s}{\mathrm{d}h} \frac{\mathrm{d}h}{\mathrm{d}\zeta} \mathrm{d}\zeta\right]
$$
(S20)

where $\Delta s_{k \to k+1}^{\mathrm{refr}} / \Delta s_{k \to k+1}$ is the correction for refraction, $\mathrm{d}s/\mathrm{d}h$ is the unrefracted path length derivative with respect to height, and $\mathrm{d}h/\mathrm{d}\zeta$ is the height derivative with respect to negative logarithm of pressure, and ζ is the negative base 10 logarithm of pressure along the LOS path s. The refraction correction is the ratio of the refracted layer path length to the unrefracted path length. The refracted path length is

$$
\Delta s_{k \to k+1}^{\mathrm{refr}} = \int_{\zeta_k}^{\zeta_{k+1}} \frac{(1+n)\,h}{\sqrt{((1+n)\,h)^2 - ((1+n_t)\,h_t)^2}} \frac{\mathrm{d}h}{\mathrm{d}\zeta} \mathrm{d}\zeta.
$$
(S21)

The absorption coefficient is a sum over each species contribution,

$$
\alpha(\nu, \mathbf{x}, \zeta) = \sum_l f^l \beta^l(T, \zeta, \nu), \quad \text{(S22)}
$$

where $\beta^l(T, \zeta, \nu)$ is species l cross section (absorption coefficient per unit volume mixing ratio, vmr), and f^l is its vmr

expressed either as a linear function,

$$f^l = \sum_m F_m^l \eta_m^l (\zeta), \qquad (S23)$$

or for upper H_2O at pressures greater than 100 hPa, as a logarithmic function,

$$f^l = \exp \left[\sum_m \ln \left(F_m^l \right) \eta_m^l (\zeta) \right], \qquad (S24)$$

where F_m^l is a mixing ratio coefficient and η_m^l is a representation basis function. The representation basis, η_m^l, is a triangular shaped function with a unit value at the coefficient break-point pressure, ζ_m, and linearly decreasing to zero at pressures ζ_{m+1} and ζ_{m-1}. These basis functions give a state vector describing linear interpolation in the vertical. Representation basis functions are discussed more fully in *Froidevaux et al.* [1996]. The linear function given in (S23) is used for all species, including upper tropospheric humidity (UTH) which has units of relative humidity with respect to ice (%RHi). However, in order to evaluate radiances, UTH needs to be transformed into vmr represented by (S24). The transformation between UTH and vmr is described more fully in *Read et al.* [2001].

The forward model calculation for all species except UTH is performed on a layered atmosphere having 91 integration layers (1 km thick between 0 and 70 km and 2 km thick from 70 to 110 km). Equation (S20) is solved with 8-point Gauss-Legendre quadrature. Radiances are computed at 81 fixed tangent heights; 10 tangents are for rays intersecting or skimming the Earth (with tangent heights from 0.0 to S100 km below the Earth surface), and 71 tangents above the Earth. The UTH retrieval uses channel 30 at 202/204 GHz, in an atmospheric window that permits measurements into the troposphere. The UTH forward model uses 35 integration layers, 19 nearly equally-spaced levels between the surface and 18 km and 16 equally-spaced levels between 20 and 50 km. Radiances are computed at 34 tangent heights above the Earth's surface and 10 Earth surface skimming and intersecting rays.

The O_2 emission in the center of band 1 is polarized because of the Earth's magnetic field. While a polarized forward model has been developed, its computational requirements prohibited its use in v5. The radiances in the center 3 channels in band 1 are therefore not used except the lowest tangent heights, for which an empirical forward model has been implemented (see section S3.9).

S3.7.4. Cross section calculations The cross section, β, in (S22) is [*Pickett et al.*, 1992]

$$\beta = \sqrt{\frac{\ln 2}{\pi}} \frac{10^{-6}}{w_d k T} P \left[\sum_j 10^{\mathscr{S}_j} \text{LineShape} \left(x_j, y_j, z_j \right) \right], \qquad (S25)$$

where

$$\mathscr{S}_j = \mathscr{S}_j (300) - \log \{ Q_{\text{ratio}} [Q (300, 225, 150), T] \} + \frac{h E l_j}{k} \left(\frac{1}{300} - \frac{1}{T} \right) + \log \left\{ \frac{1 - \exp \left[-h\nu_j / kT \right]}{1 - \exp \left[-h\nu_j / k(300) \right]} \right\}, \qquad (S26)$$

T is temperature in Kelvins, $P \ (= 10^{-\zeta})$ is pressure in hPa, $\mathscr{S}_j (300)$ is the logarithm of the integrated intensity in nm^2 MHz at 300 K, ν_j is the pressure shifted line center frequency in MHz, El_j is the lower state energy in cm^{-1}, $\log \{Q_{\text{ratio}}\}$ is the logarithm of the ratio of the partition function at T to the partition function at 300 K, $Q (300, 225, 150)$ are values of the partition function at 300, 225, and 150 K, and h and k are Planck and Boltzmann constants, respectively. The partition function ratio is evaluated with a linear interpolation of the logarithm of the partition functions and the logarithm of temperature. The spectral parameters, $\mathscr{S}_j (300)$, $Q (300, 225, 150)$, El_j, and ν_j are taken from the JPL submillimeter, millimeter, and microwave spectral line catalog [*Pickett et al.*, 1992].

$$w_d = \frac{\nu_j \sqrt{2 \ln 2 k T}}{c \sqrt{\mathcal{M}}} \qquad (S27)$$

is the Doppler width in MHz, $\mathcal{M}$ is the absorber molecular mass in amu, and j identifies the individual lines or quantum states in the molecule, and c is the speed of light. The line shape function is a convolution of a collision contribution [*vanVleck and Weisskopf*, 1945] and a velocity broadening (Doppler) contribution,

$$\text{LineShape} \left(x_j, y_j, z_j \right) = \left(\frac{\nu}{\nu_j} \right)^2$$
$$\times \left\{ \frac{1}{\pi} \int_{-\infty}^{\infty} \frac{\left[y_j - Y_j \left(x_j - t \right) \right] \exp \left(-t^2 \right)}{y_j^2 + \left(x_j - t \right)^2} dt \right.$$
$$\left. + \frac{1}{\sqrt{\pi}} \frac{y_j - Y_j z_j}{z_j^2 + y_j^2} \right\},$$

where

$$x_j = \frac{\sqrt{\ln 2}\,(\nu_j - \nu)}{w_d},$$

$$y_j = \frac{\sqrt{\ln 2}\,w_{cj} P \left(\frac{300}{T}\right)^{n_j}}{w_d},$$

$$z_j = \frac{\sqrt{\ln 2}\,(\nu_j + \nu)}{w_d}.$$

w_{cj} is the collision width in MHz hPa^{-1} at 300 K, n_j is its temperature dependence, Y_j is an intramolecular line mixing contribution, ν_j is the line position frequency in MHz, ν is the radiation frequency in MHz. The $(\nu/\nu_j)^2$ term, which is virtually constant over a Doppler width, has been pulled outside the integral, giving the well studied Voigt integral [*Shippony and Read*, 1993, 2002]. The line center frequency is pressure shifted according to

$$\nu_j = \nu_{j_0} + \Delta\nu_{j_0} P \left(\frac{300}{T}\right)^{\frac{1+6n_j}{4}}, \qquad (S28)$$

where ν_{j_0} is the 'zero pressure' line center frequency in MHz, $\Delta\nu_{j_0}$ is the pressure shift parameter in MHz hPa^{-1} at 300 K, and the temperature dependence is related to n_j [*Pickett*, 1980]. The intramolecular line mixing contribution is parameterized according to

$$Y_j = P \left[\delta_j \left(\frac{300}{T}\right)^{0.8} + \gamma_j \left(\frac{300}{T}\right)^{1.8} \right] \qquad (S29)$$

where δ_j and γ_j are line-mixing coefficients in hPa^{-1} at 300 K. The linewidth parameters, w_{cj} and n_j, are based on laboratory measurements. The line shift, $\Delta\nu_{j_0}$, is nonzero only for H_2O [*Pumphrey and Bühler*, 2000]. The line mixing coefficients are nonzero only for O_2 [*Liebe et al.*, 1992].

For the pre-frequency-averaged calculations, cross sections and their derivatives are computed on a molecule by molecule basis. The contributions from each line inside the MLS band, wings of strong lines outside the band, and background continuum [*Read et al.*, 2001] are summed and weighted by the MLS filter response function to produce a cross section for each channel. These are computed for a range of temperatures and pressures and stored in tables. The temperature dependence of β is approximated with

$$\beta = \beta (300) (300/T)^n \qquad (S30)$$

and n is computed and stored. Also computed is $d\beta/d\nu$, the derivative of channel cross section with respect to molecular velocity. This is used for computing the radiance derivative with respect to molecular velocity.

For situations where the radiances are frequency averaged, the cross section is computed as needed. The calculation includes only those lines within the band for each species under consideration and approximates contributions from strong line wings and its continuum with an empirical polynomial function of pressure and temperature. The line data, ν_{j_0}, El_j, $\mathscr{S}_j$ (300), w_{cj}, n_j, Y_j, and $\Delta\nu_{j_0}$, and coefficients of the polynomial function are stored in a file cataloged by species and MLS band that is read by the forward model program if needed.

The UTH forward model described in detail by *Read et al.* [2001] uses spectrally averaged cross sections. H_2O and air cross sections are empirical continuum functions determined from in-orbit data. Cross sections for the contributing species O_3, N_2O, and HNO_3 are computed from a line by line calculation.

S3.7.5. Forward model derivatives   In addition to radiances, the forward model computes radiance derivatives with respect to the state vector for use in the retrieval. As with radiance calculations, this is a three part calculation including FOV and spectral integrations and a radiative transfer derivative calculation.

The FOV radiance derivative calculation is given by:

$$\frac{\partial \hat{I}_{ch}^L}{\partial x_j} = \int_{-\infty}^{\infty} \left[\frac{\partial \overline{I}_{ch}^L}{\partial x_j} + \overline{I}_{ch}^L \frac{\partial}{\partial \chi} \left(\frac{\partial \chi}{\partial x_j} \right) \right] G\left(\chi_t - \chi\right) d\chi$$
$$+ \frac{\partial \chi_t}{\partial x_j} \int_{-\infty}^{\infty} \overline{I}_{ch}^L \frac{\partial G\left(\chi_t - \chi\right)}{\partial \left(\chi_t - \chi\right)} d\chi$$
$$- \int_{-\infty}^{\infty} \overline{I}_{ch}^L \frac{\partial \chi}{\partial x_j} \frac{\partial G\left(\chi_t - \chi\right)}{\partial \left(\chi_t - \chi\right)} d\chi. \quad (S31)$$

The multiterm equation involving derivatives of the antenna gain function, $G\left(\chi_t - \chi\right)$, as well as the spectrally integrated derivatives of the radiative transfer function, $\overline{I}_{ch}^L$, is a consequence of using pressure as the independent vertical coordinate. The FOV function varies with some state vector components when projected onto the vertical coordinate system. Referring to (S14), the elements of $\mathbf{x}$ which have nonzero $\partial \chi/\partial x_j$ are temperature, T, Earth radius, $h_\oplus$, and satellite radius, h_s (the dependencies of n are neglected).

The partial derivatives for these terms are,

$$\frac{\partial \chi}{\partial T_m} = \frac{\tan \chi}{h_c} \frac{dh_c}{dT_m},$$

$$\frac{\partial}{\partial \chi} \left(\frac{\partial \chi}{\partial T_m} \right) = \frac{2 + \tan^2 \chi}{h_c} \frac{dh_c}{dT_m} + \frac{\eta_m^T}{T},$$

$$\frac{\partial \chi}{\partial h_s} = -\frac{\tan \chi}{h_s},$$

$$\frac{\partial}{\partial \chi} \left(\frac{\partial \chi}{\partial h_s} \right) = -\frac{1}{h_s \cos^2 \chi},$$

$$\frac{\partial \chi}{\partial h_\oplus} = \frac{\tan \chi}{h_c}, \text{ and}$$

$$\frac{\partial}{\partial \chi} \left(\frac{\partial \chi}{\partial h_\oplus} \right) = \frac{1}{h_c \cos^2 \chi}, \qquad \text{(S32)}$$

where T_m is a coefficient in the temperature profile. The derivative, $\partial G [\chi_t - \chi] / \partial [\chi_t - \chi]$ is evaluated using the Fourier transform derivative property

$$\mathcal{F} \left(\frac{\partial G(\chi)}{\partial \chi} \right) = iq \mathcal{F} (G(\chi)) \qquad \text{(S33)}$$

where q is the aperture coordinate (number of wavelengths) and $i = \sqrt{-1}$. This property is convenient because the pattern is stored as $\mathcal{F}[G(\chi)]$ which ensures internal consistency between the pattern and its derivative. The integrals in (S31) are evaluated with Fourier transforms analogous to (S13).

The spectral integration of the radiance derivatives is identical to (S16) used for radiances, with $\frac{\partial \overline{I}_{\mathrm{ch}}^{\mathrm{L}}}{\partial x_j}$ and $\frac{dI_t}{dx_j}$ replacing $\overline{I}_{\mathrm{ch}}^{\mathrm{L}}$ and I_t. However, derivatives for all channels are computed with spectrally integrated 'cross sections' (i.e., 'pre-frequency-averaging approximation'). This reduces the number of spectral radiance derivative calculations to one per channel. For those cases where the radiances are computed from a spectral integration of multiple radiative transfer calculations per channel, the derivative is scaled by the ratio of the spectrally integrated radiance to the radiance computed from a spectrally integrated cross section. In most cases, this approximation produces very good results.

The derivative of the radiative transfer equation with re-spect to a state vector element is

$$\frac{dI_t}{dx_j} \equiv K_{tj} =$$

$$\sum_{i=t}^{N} \left(\frac{d\Delta B_i}{dx_j} + \Delta B_i \sum_{k=i}^{N-1} \frac{d\Delta \delta_{kt}}{dx_j} \right) \prod_{k=i}^{N-1} \Delta \tau_{kt}$$

$$- \Upsilon \left(\prod_{k=t}^{N-1} \Delta \tau_{kt} \sum_{k=t}^{N-1} \frac{d\Delta \delta_{kt}}{dx_j} \right)$$

$$\times \left[\sum_{i=t}^{N} \left(\frac{d\Delta B_i}{dx_j} + \Delta B_i \sum_{k=t}^{i-1} \frac{d\Delta \delta_{kt}}{dx_j} \right) \prod_{k=t}^{i-1} \Delta \tau_{kt} \right.$$

$$\left. - 2I_o \left(\prod_{k=t}^{N-1} \Delta \tau_{kt} \right) \right], \quad \text{(S34)}$$

where $d\Delta \delta_{kt}/dx_j$ is the derivative of the layer opacity (the argument of the exponential function in (S20)) with respect to state vector element x_j, and $d\Delta B_i/dx_j$, is the derivative of ΔB_i with respect to state vector element x_j which is zero except for temperature. The layer opacity derivatives are evaluated analytically for each state vector element. The value for any sum term that does not exist (e.g., when $i = N$ in the second sum in the first term and $i = t$ in the second sum of the third term) is zero.

S3.7.6. Forward model implementation in retrievals
The forward model described above is a very complex and time consuming calculation. It was not possible to implement this full calculation operationally for all the MLS channels. Instead a linear approximation to (S12) from a Taylor series is implemented, according to:

$$\hat{I}_{\mathrm{ch}}^{\mathrm{L_0}} = r_u \left[I_{\mathrm{ch},u}^{\star \mathrm{L_0}} + \mathbf{K}_{\mathrm{ch},u}^{\star \mathrm{L_0}} (\hat{\mathbf{x}} - \mathbf{x}^\star) \right]$$

$$+ r_l \left[I_{\mathrm{ch},l}^{\star \mathrm{L}} + \mathbf{K}_{\mathrm{ch},l}^{\star \mathrm{L_0}} (\hat{\mathbf{x}} - \mathbf{x}^\star) \right]. \quad \text{(S35)}$$

The full forward model is used to compute values of $I^{\star L_0}$ and $\mathbf{K}^{\star L_0}$ for upper and lower sidebands of each channel, corresponding to observations made at a fixed set of tangent pressures (denoted by L_0), based on a representative state $\mathbf{x}^\star$. In the v5 processing, the Taylor series in (S35) is computed, followed by an interpolation of the resulting radiance profile to the tangent pressures given in the state vector. In addition, the pretabulated $\mathbf{K}^\star$s are combined by sideband, and also interpolated to the state vector tangent pressures. While the radiances are interpolated using a cubic spline [*de Boor*, 1987], the weighting function matrix values are interpolated linearly.

The accuracy of the linear approximation is dependent on the proximity of the state $\mathbf{x}$ to the representative state

$\mathbf{x}^{\star}$. Accordingly, representative values of $\mathbf{x}^{\star}$ have been chosen for several 'bins'. The divisions of the bins are the 'UARS months' (10 per calendar year); 8 latitude regions with boundaries at the equator, $\pm 20°$, $\pm 40°$, and $\pm 60°$; and the ascending and descending sides of the orbit (needed to account for Doppler shift effects). The values for species abundances and temperatures in the $\mathbf{x}^{\star}$ vector for each bin are taken from appropriate climatology.

One indicator of the accuracy of the linear forward model is optical depth $\tau_{\mathrm{ch}}^{\mathrm{L}}$, which is estimated for each sideband from calculated radiances using

$$\tau_{\mathrm{ch}}^{\mathrm{L}} \simeq -\ln\left[1 - \frac{\hat{I}_{\mathrm{ch}}^{\mathrm{L}}}{T^{\mathrm{L}}}\right], \qquad (\mathrm{S}36)$$

where T^{L} is the atmospheric temperature at the tangent point. Section S4 discusses the use of the optical depth as an indicator of linear forward model radiance quality in the v5 algorithms.

For most of the MLS observations the linear forward model is a very good approximation, particularly for bands 2–4, where the signals are never optically thick in the stratosphere. It is also a good approximation for band 1, despite the very optically-thick nature of these signals, because temperature and pressure—not mixing ratio—are retrieved from the band 1 radiances. Temperature has a fairly linear effect on the signals, and the nonlinear effects of tangent pressure are described well by the cubic spline interpolation in tangent pressure performed by the linear forward model.

Bands 5 and 6 show significant nonlinear effects, as the channels become increasingly optically thick closer to the line center, and lower in the atmosphere. Radiances in channels close to the line centers are ignored when the optical depth in either sideband is greater than a certain threshold. However, information can still be obtained from other channels at the same tangent altitudes, as the linear forward model is still applicable to channels further away from the line center. In the lower stratosphere however, the only information comes from the 'wing' channels, and the full nonlinear model has to be used. For reasons of efficiency, only the radiances are computed with the nonlinear model; derivatives of radiance with respect to mixing ratio are still obtained from the linear model.

The UTH retrieval is based on fitting the radiances in a single channel as described in [*Read et al.*, 2001]. The UTH retrieval is sufficiently nonlinear that the full forward model computation, with derivatives, is implemented. However, as only a single channel is used, over a small vertical range, the computational effort required is not prohibitive.

S3.8. The 'scan residual' model

In addition to radiance information, the estimates of limb tangent point altitudes (based on the MLS antenna position encoder readouts and the spacecraft attitude determination system) are used as additional measurements in the retrieval of temperature, pressure, and geopotential height. The forward model for these measurements consists of a hydrostatic calculation of the tangent point altitudes, based on the values of tangent point pressure, temperature and the geopotential height of a reference pressure surface, taken from the state vector. Complexities in this approach arise from the variations in the Earth's gravitational field with altitude and latitude.

Expressing the problem in terms of geopotential rather than geometric height simplifies the calculations. The hydrostatic calculation assumes that the atmosphere is an ideal gas with the gas 'constant' described as a function of $\zeta = -\log_{10}\left[\text{pressure} / \text{hPa}\right]$ by

$$R(\zeta) = \frac{R_0}{M}, \qquad (\mathrm{S}37)$$

where R_0 is the ideal gas constant and the molecular mass

$$M = 0.0289644 \cos\left(0.2\left[\zeta' - \zeta_c\right]\right), \qquad (\mathrm{S}38)$$

with $\zeta' = \max(\zeta, \zeta_c)$, and $\zeta_c = 2.5$, describes a fit to the US Standard Atmosphere. An exact integration is used, although for simplicity linear variation in RT across each layer is assumed, (as opposed to linear variation in T with the variation in R described in full by (S37)). The same integration is used to produce vertical profiles of geopotential height from the reference geopotential height and temperature information that are the geopotential height product.

There are many well-documented expressions for converting geometric height to geopotential height [*Tscherning*, 1984]. V5 uses the expression

$$H_\infty = \frac{GM}{g_0 h_c}\left[1 - J_2 P_2\left(\lambda_c\right)\left(\frac{a}{h_c}\right)^2 - J_4 P_4\left(\lambda_c\right)\left(\frac{a}{h_c}\right)^4\right] + \frac{\omega^2 h_c^2 \cos^2\left(\lambda_c\right)}{2 g_0}, \quad (\mathrm{S}39)$$

with

$$P_2\left(\lambda_c\right) = \frac{1}{2}\left(3\sin^2\left(\lambda_c\right) - 1\right)$$

$$P_4\left(\lambda_c\right) = \frac{1}{8}\left(35\sin^4\left(\lambda_c\right) - 30\sin^2\left(\lambda_c\right) + 3\right),$$

where $a = 6378137.0\,\mathrm{m}$ is the assumed Earth major axis, $\omega = 7.292115 \times 10^{-5}\,\mathrm{s}^{-1}$ is the Earth angular velocity, and

$GM = 3.986005 \times 10^{14}\,\mathrm{m^3 s^{-2}}$. $J_2 = 1.0826256 \times 10^{-3}$, and $J_4 = -2.3709122 \times 10^{-5}$ are polynomial terms, λ_c is geocentric latitude, h_c is geocentric altitude, and $g_0 = 9.80665\,\mathrm{m s^{-2}}$ is the nominal gravitational acceleration. The geodetic altitude reported by the UARS orbit/attitude software is simply the difference between the geocentric altitude and local Earth radius, not the 'proper' geodetic altitude. Its conversion back to geocentric altitude therefore makes the same approximation.

A further subtlety arises from the effects of refraction on the limb rays. The tangent point pressure terms in the state vector describe the pressure at the true tangent points, whereas the level 1 tangent point altitudes that are input to the level 2 processing refer to fictitious rays not affected by refraction. The effects of refraction are taken into account and the altitudes modified according to

$$h_c = \frac{h_c^u}{1+n}, \qquad (S40)$$

where n is given by (S15).

The effects of refraction make the mathematical construction of the retrieval problem a little more complex. If we still wish to consider the system in terms of geopotential height, a conceptual problem arises, as the 'measurements' of refracted geopotential height are dependent on the contents of the state vector (through the temperature and water vapor terms in (S15)). Typically, only the forward model estimates are affected by changes in state vector values. To avoid this (merely semantic) issue, we reformulate the problem in terms of a 'scan residual', defined as the difference between the geometric and hydrostatic geopotential heights. The 'measurements' of this quantity are defined to be zero, with appropriate precisions based on estimates of pointing uncertainty. In addition to computing this residual quantity, the model also computes its derivative with respect to temperature, tangent pressure and reference geopotential height for use in the retrieval algorithm.

Including the scan model requires that the retrieval algorithms not use virtual measurements for tangent pressure, as these would be based on the same tangent height information being used by the scan model. It can be shown that the scan model provides enough information to ensure that the matrix in (S5) can be inverted.

These calculations also form the basis of a 'first guess' solver for the tangent pressure. This takes the a priori temperature and reference geopotential height and computes an initial guess for the tangent pressure, based on the observed tangent point geometric altitudes.

S3.9. An empirical model to improve mesospheric pressure and temperature

In order to improve estimates of tangent pressure in the mesosphere, the v5 algorithms implement an approximate retrieval of mesospheric temperature and pressure, using an empirically-derived forward model for the saturated (sometimes described as 'blacked out') radiances at the lowest tangent point in each scan from the three center channels (7–9) in the 63-GHz radiometer. The value of a saturated radiance reflects the temperature in the region of the mesosphere where the saturation occurs. However, the altitude of saturation (i.e., where the temperature weighting function peaks) is strongly affected by the geomagnetic field, due to the Zeeman splitting of the 63-GHz O_2 emission. A full polarized forward model calculation was too computationally expensive to implement for v5. Instead an empirical model was developed.

Study has shown that the temperature weighting function mimics the shape of the radiance derivative with respect to tangent height, offset by $\sim 8\,\mathrm{km}$. This can be used to obtain an empirical estimate of the weighting function directly from the limb radiances observed within each scan. First, the radiance derivatives with respect to tangent height are computed in the normal scan range (0–90 km). Above this range a linear decay to zero at 120 km is assumed. Secondly, the derivative profile is normalized and shifted down by $\sim 8\,\mathrm{km}$, giving an approximate weighting function. Thirdly, weighting functions are multiplied by the state vector temperature profile to determine the model saturated radiances. No mesospheric retrieval is attempted if the scan does not reach 80 km.

Using this empirical model, v5 produces estimates of mesospheric temperature that represent an improvement on the a priori information (based on the UARS zonal mean climatology). While this 'improved' mesospheric temperature does lead to better retrievals mesospheric tangent pressure (through the hydrostatic balance imposed by the scan model described in section S3.8), the resulting mesospheric temperatures are not considered useful for scientific study (see section S7.1). The empirical approach is not applicable to unsaturated radiances, as these are more strongly influenced by the Zeeman effect.

S3.10. Differences from earlier algorithms

The v5 algorithms represent a departure from previous approaches to the UARS MLS Level 2 processing. Earlier versions used sequential estimation *Rodgers* [1976] to retrieve the state of the atmosphere, invoking the Taylor series forward model only, introducing radiances one at a time starting with those measured at the top of the scan. The

earlier algorithms performed the retrieval tasks in similar phases to v5, however, only diagonal propogation was used for uncertainties in constrained quantities. There was no 'scan model' in the earlier versions (see section S3.8), instead, the geometric tangent height information was used to obtain an a priori for tangent pressure.

S4. Implementation of algorithms

There are several configurations of the algorithms, corresponding to different operational modes of the MLS instrument. The changes in instrument operation that necessitated configuration modifications were the April 1993 failure of the 183-GHz radiometer and the cessation in June 1997 of 63-GHz radiometer observations (to conserve spacecraft power). This section first describes factors common to all configurations, and then discusses specific details of each configuration.

S4.1. Sources of a priori data

Each element of the state vector is initialized before the retrieval with a priori information. This includes not only the retrieved species such as temperature, ozone, etc., but also contaminating species such as N_2O. Furthermore, for all the retrieved species, except tangent pressure (for reasons described above), this a priori value is also used as a virtual measurement, as described in section S3.2. The a priori data for most species come from the UARS standard climatology. Note that this is the climatology constructed before launch for UARS data processing, not the climatology later constructed using UARS data (the UARS Reference Atmosphere Project, [*Wang et al.*, 1999, for example]). In the case of water vapor, the climatology has been modified in the manner described in *Pumphrey et al.* [1998].

The temperatures in the state vector are initialized with data from the National Centers for Environmental Prediction (NCEP, formerly NMC) Global Data Assimilation System (GDAS) Stratospheric Analysis data. These data are typically available up to ~0.3 hPa, though occasionally they are missing at lower altitudes, or for a complete day. Where NCEP data are not available, data from the UARS climatology are used. The 100-hPa geopotential height is also initialized with NCEP data if available, with the UARS climatology as a fall back.

S4.2. Retrieval ranges and a priori covariances

Table S13 describes the vertical range over which each species was retrieved and gives the values used for the a priori error estimates. The latter were chosen based on lenient estimates of the amounts of variability to be expected in the

atmosphere and an examination of the results of many test runs of the data processing algorithms.

The choice of 20 km for most products for the correlation length scale in Equation S8, described in section S3.2 (strictly speaking this is a length in pressure space) deserves some explanation. Firstly, this is not a smoothing length or vertical resolution that is directly imposed on the retrieval. It is a parameter applied to the a priori covariance matrix that makes vertically-correlated solutions more attractive. The correlation length was initially chosen based on studies of the ClO product, which has a fairly poor signal-to-noise ratio. A 20-km length was found to yield ClO profiles with suitable signal to noise for daily mapped products, with vertical resolution of 4–5 km in the lower stratosphere (see section 13).

Tests showed that the choice of correlation length had little impact on retrievals of other species, except for temperature and upper tropospheric humidity. Therefore, for simplicity, 20 km was chosen as the length scale for all the remaining species. However, this length scale was later found to have some undesirable side effects. In particular, as described in section 6.1, the retrieval overestimates the random uncertainty in the data.

S4.3. Data from launch to June 14, 1997

For the processing of data from launch to June 14, 1997, the configuration of the v5 algorithms is essentially the same for each day processed. The only major change in is that necessitated by the April 1993 failure of the 183-GHz radiometer, described below.

S4.3.1. 63-GHz retrievals The first phase consists of a retrieval of temperature, tangent point pressure and 100-hPa geopotential height, using the radiances from the 63-GHz radiometer and the estimates of tangent point altitude obtained by the Level 1 processing.

This phase implements three forward models. The first is the linearized model, used for all radiances from channels 1–6 and 10–15. This includes emissions from $^{16}O_2$, $^{18}O^{16}O$, and $^{17}O^{16}O$. Continuum emissions from N_2 and H_2O contribute negligibly to total emission in this band and are not included. The O_2 volume mixing ratio used is 0.2095 from the surface to 80 km with a linear decrease to 0.1447 at 110 km. The 18 and 17 isotopic forms have mixing ratios scaled by 4.07×10^{-3} and 7.5×10^{-4}, respectively.

The scan model described in section S3.8 is used. A 100 m precision is assumed for the input residuals. The empirical mesospheric model described in section S3.9 is also used for the radiances from the lowest tangent height minor frame for channels 7–9. A Gauss-Newton iterative retrieval with a maximum of four iterations is used.

Table S13. Retrieval ranges and a priori information for all the v5 data products.

Species	Vertical range[a]	A priori source	A priori error	Correlation length
Temperature	68 – 0.0001 hPa	NMC data, with UARS climatology stacked above	10 – 46 K	~5 km
Upper Tropospheric Humidity	464 – 146 hPa	50% global RHi	150% RHi	~3 km
Stratospheric water vapor (H_2O)	100 – 0.00046 hPa	UARS climatology	20 ppmv	~20 km
183-GHz Ozone (O_3)	100 – 0.00046 hPa	UARS climatology	20 ppmv	~20 km
205-GHz Ozone (O_3)	100 – 0.00046 hPa	UARS climatology	20 ppmv	~20 km
Nitric acid (HNO_3)	100 – 0.46 hPa	UARS climatology	10 ppbv	~20 km
Chlorine monoxide (ClO)	100 – 0.46 hPa	UARS climatology	4 ppbv	~20 km
Methyl cyanide (CH_3CN)	100 – 0.14 hPa	UARS climatology	500 pptv	~20 km

[a] This is the range for which data are retrieved, not the range over which they are considered useful, nor the range over which data are output.

As described in section S3.6, in addition to temperature, tangent pressure and reference geopotential height, a minor-frame-dependent radiance baseline is retrieved. This is different from the other bands, where scan-independent baselines are retrieved along with atmospheric extinction profiles. This method was chosen as it led to better radiance fits than the extinction approach.

S4.3.2. Upper tropospheric humidity retrievals The retrieval of upper tropospheric humidity consists of three phases, the first two of which are performed immediately following the retrieval of temperature, tangent pressure and geopotential height. The first is a retrieval of a layer mean humidity from 464 to 147 hPa that provides an initial guess for the UTH profile retrieval. The second phase is a retrieval of humidity on the four UARS surfaces from 464 to 147 hPa. The forward model for the UTH retrieval includes emissions from dry and moist continua and O_3, HNO_3, and N_2O, taken from the state vector. In the first and second UTH retrieval phases, the O_3 and HNO_3 concentrations are given by a priori. Once better estimates of these have been obtained from later retrieval phases, a third UTH retrieval phase is performed to improve the accuracy of the UTH data.

The UTH retrieval is split in this manner because it was found that having good estimates of UTH improved the quality of the retrievals of other species in the lower stratosphere. Thus the first two phases are designed to obtain an interim estimate of UTH, sufficient for use in the stratospheric retrievals.

The UTH retrieval is generally similar to that of version 4.9 (v4.9) [*Read et al.*, 2001]. The main differences are:

1. V4.9 software took temperature from the NCEP dataset, on the original NCEP pressure grid. V5 uses the state vector temperatures, which are NCEP data interpolated to the UARS pressure levels, with UARS climatology substituted in regions where NCEP data

are unavailable. V4.9 did not perform retrievals where NCEP data were unavailable.

2. The off-diagonal terms in the a priori covariance matrix had a Gaussian form in v4.9, as opposed to the exponential form given in Equation (S8).

3. V4.9 used a different form for the wet and dry continua from that used by v5. This is discussed in section 9.

4. The v4.9 retrieval constrained O_3 and HNO_3 values to version 4 data. V5 uses the retrieved v5 values of O_3 and HNO_3, as described above.

5. V4.9 retrieved UTH only when there were four or more radiance observations at tangent pressures greater than 80 hPa. V5 undertakes retrievals whenever any radiances meet this criterion.

S4.3.3. 183-GHz retrievals The next phase is the retrieval of stratospheric water vapor and 183-GHz ozone from the two 183-GHz bands. Band 5 (channels 60 – 75) is centered on the 183.310-GHz H_2O line and band 6 (channels 76 – 90) on the 184.377-GHz O_3 line. Channel 69, close to the center of the H_2O line, is not used because of unexplained systematic biases seen in the radiances, thought to be instrumental artifacts. Also, channel 76, on the ozone line wing, is not used as its radiances are unreliable. For the center 9 channels of each band, radiances are only used if the tangent point pressure is smaller than 100 hPa and the optical depth in each sideband is less than 1.0. For these channels, the linear forward model is used to estimate radiances and weighting functions. For the sets of three channels at either end of each band (excluding channel 76), a nonlinear forward model is used to compute radiances (weighting functions are still obtained from the linear forward model, and therefore do not change with each iteration). In these chan-

nels all radiances whose tangent point pressures are smaller than 100 hPa are used.

The forward model for both bands 5 and 6 includes emissions from H_2O, O_3, dry air continuum, and extinction. The dry continuum function is the same as that used for the UTH retrieval with an empirical frequency adjustment based on N_2 collision-induced absorption data [*Read et al.*, 2001]. In addition to retrieving stratospheric water vapor and 183-GHz ozone, spectrally-flat extinction coefficients and baselines are retrieved independently for bands 5 and 6, as described in section S3.6.

The forward models take the temperature, pressure and upper tropospheric humidity from the results of earlier phases. As described in section S3.3, the effects of uncertainty in retrieved temperature and tangent pressure are propagated into the band 5 and 6 radiance error budgets. For speed, off-diagonal terms in the covariance matrices are ignored for all radiances having tangent pressures smaller than 22 hPa. An iterative retrieval based on the Marquardt-Levenberg method is used.

This phase is not invoked for data obtained after the April 1993 failure of the 183-GHz radiometer. The stratospheric water vapor and 183-GHz ozone elements of the state vector for these later days are therefore unchanged from their a priori values.

S4.3.4. 205-GHz retrievals The 205-GHz radiometer data (bands $2-4$, channels $16-60$) are used to retrieve 205-GHz ozone, chlorine monoxide, nitric acid, and methyl cyanide. In addition to these species, baseline and extinction are retrieved jointly for the overlapping bands 2 and 3, with a separate baseline and extinction retrieved for band 4. All the radiance observations in each band with tangent pressures less than 150 hPa are used in the retrieval. As this system is very linear, only a single iteration is performed.

The forward model includes the following species for bands 2 and 3: ^{35}ClO, HNO_3, H_2O_2, SO_2, O_3, $^{18}OO_2$, $H_2{}^{18}O$, N_2O, $O_3(\nu2)$, CH_3CN, wet continuum, dry continuum, baseline and spectrally flat extinction. The band 4 forward model includes emissions from O_3, HNO_3, SO_2, $O^{18}OO$, N_2O, HO_2, $O_3(\nu2)$, wet continuum, dry continuum, spectrally flat extinction and baseline. A priori values are used for species not retrieved. Note that this includes species that are related to retrieved quantities, such as ozone isotopes and excited states. This is a departure from version 4, in which such species were appropriately constrained to the retrieved value of the 'parent' species. The v4 approach would have led to more accurate results, however, it could not be implemented in the v5 software.

In earlier versions of the MLS software, SO_2 was retrieved from these bands [*Read et al.*, 1993]. However, the

algorithms retrieved small but unrealistic SO_2 mixing ratios in the atmosphere at times when SO_2 abundance was not enhanced by volcanic injections. Studies showed that the band 2 and 3 radiances exhibited a persistent spectral feature, similar to SO_2, that accounted for this bias. This spectral feature is now known to be emission from CH_3CN [*Livesey et al.*, 2001]. It was decided in v5 to retrieve CH_3CN instead of SO_2, constraining SO_2 to a climatological field. Their spectral similarity in the UARS MLS bands makes simultaneous retrieval of SO_2 and CH_3CN inappropriate.

In the absence of volcanic contributions, stratospheric SO_2 has a typical abundance of $\sim$0.1 ppbv or less [*Brasseur and Solmon*, 1986], corresponding to a signal of $\sim$0.01 K [*Read et al.*, 1993]. This compares to a typical CH_3CN signal of $\sim$0.5 K [*Livesey et al.*, 2001]. Excluding times of volcanic activity therefore, variations in SO_2 abundance (assumed constant in the retrieval algorithm) will have negligible impact on retrieved CH_3CN. However, when SO_2 loading is high, especially in the months following the Mt. Pinatubo eruption, biases will arise in the CH_3CN data due to the large SO_2 signals, as discussed in section 15.

As in the previous phase, the effects of uncertainty in retrieved temperature and tangent pressure were propagated into the error budget, with full propagation for radiances in bands 2 and 4 with tangent pressures greater than 22 hPa, and diagonal propagation elsewhere. In addition the uncertainty in H_2O (taken from the earlier phases, or a priori for the stratosphere and mesosphere following the 183-GHz failure) was also accounted for.

Note that the forward model and retrieval consider emission from the ^{35}ClO isotope. Before output, the retrieved mixing ratios are scaled by 1.32 to produce the combined abundance of the ^{35}ClO and ^{37}ClO isotopes. This phase is followed by the final UTH retrieval phase, as described above.

S4.4. Data from 15 June 1997 onward

From June 1997, in order to conserve spacecraft power, the instrument was operated with only the 205-GHz radiometer. The data from this period are processed in v5 by implementing a single-phase retrieval of all the 205-GHz products as described above, with the addition of limb tangent pressure, for which information is obtained from the width of the 206-GHz O_3 line. The temperature is constrained to a priori (i.e., NCEP or climatology). In addition to the bands 2, 3 and 4 radiance measurements above 150 hPa, the tangent point altitudes are also used, with the scan model described in section S3.8. No constrained quantity error propagation is needed. A nonlinear iterative retrieval is used with the Marquardt-Levenberg methodology.

This is followed by a two-phase UTH retrieval, identical to the first and third UTH phases in the 'standard' processing.

S5. Proper use of MLS data

No supplementary material.

S6. Validation and characterization issues common to all species

S6.1. Effects of the cessation of 63-GHz radiometer observations

As stated in section S4.4, after June 1997 MLS was operated without the 63-GHz radiometer. The v5 algorithms were modified for data taken after June 1997. The impact this modification had on the data was assessed by running these modified algorithms on data from selected days earlier in the mission and comparing the results with the 'standard' v5 data. This was done for observations on January 4, January 29, March 16, April 25, June 12, July 5, August 20, September 27, October 23, and December 13, all 1996. The results of this exercise are given in later sections describing individual species.

Although the use of a different retrieval configuration resulted in slight changes in behavior for χ^2 quantities, the criteria for setting values for flags such as `QUALITY_03_205` were not changed between the two implementations of the algorithm. This results in generally less-cautious quality control (i.e., fewer profiles are rejected) for the post-June 1997 data.

S6.2. Retrieved tangent pressure

As described in section S3.6, one of the most important components of the state vector for v5, apart from the 'products', is the set of tangent point pressures for each minor frame of observation. Figure S11 shows a summary of the estimated tangent pressure precision (from Equation (S6)). It is clear that the precision of v5 tangent pressure is significantly improved over the v4 data. This is due to the introduction of the scan model (section S3.8). Also, it is interesting to note the change of behavior resulting from the switch to observations from the 205-GHz radiometer alone (section S6.1). The 63-GHz observations yield information mainly on the state of the upper stratosphere and lower mesosphere, whereas the 206-GHz ozone signal, being the emission from a weaker line, conveys useful tangent pressure information down to the lower stratosphere.

As described in section 4 these estimated precisions are carried forward into the error budgets for the retrievals of the
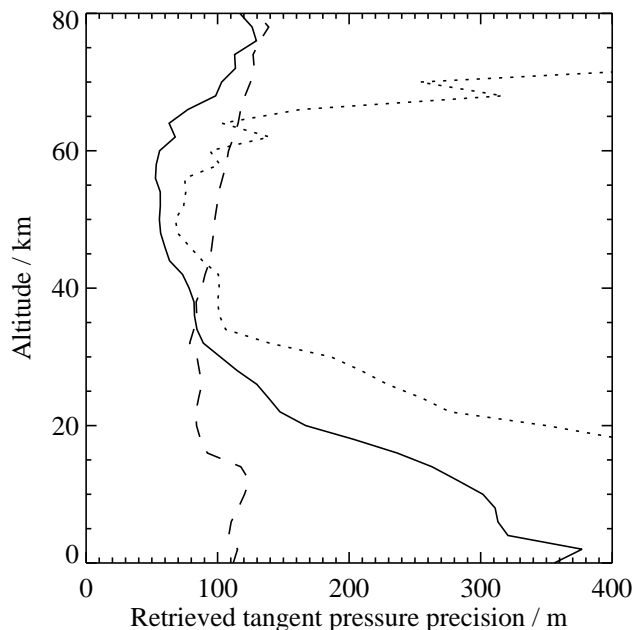
Figure S11. Typical precision for retrieved tangent pressure. The solid line shows the mean estimated precision in v5 retrieved tangent pressure on June 14, 1997 (converted into approximate meters using a $16\,km \log_{10}$ scale height). The dotted line shows the same information for v4. The broken line indicates the same statistic for the v5 retrieval of data taken on July 14, 1997, a day when only the 205 GHz radiometer was activated.

atmospheric species.

S7. Temperature

S7.1. Mesospheric Temperature

As discussed in section S3.9 the v5 algorithm employs an empirical forward model to obtain information on mesospheric temperature (at pressures <0.32 hPa). Table S14 summarizes the estimated vertical resolution and single profile precision for the mesospheric temperature. The significant contributions of the a priori information to the mesospheric temperatures necessitate a different measure of the precision of the dataset from that used for other products. An approximate measure s_m can be obtained from

$$\frac{1}{s_m^2} = \frac{1}{s_x^2} - \frac{1}{s_a^2}, \tag{S41}$$

where s_x is the precision quoted in the Level 3AT files, and s_a is the a priori precision. s_m is an approximate measure of the precision of the information MLS contributed to the

retrieval system. The overall accuracy of these data remains to be assessed.

Table S14 also gives differences between v5 and the Improved Stratospheric and Mesospheric Sounder (ISAMS) v12 temperature observations during December 4, 1991 and January 14, 1992. The preliminary comparisons show that MLS temperatures are generally warmer than those from ISAMS at these altitudes. The warm bias increases with height from ~1 K at 0.32 hPa to ~10 K at 0.01 hPa. Comparisons of ISAMS data with lidar observations [*Dudhia and Livesey*, 1996] indicate that there is good agreement between MLS and lidar at 0.3–0.03 hPa.

Figure S12 compares MLS and ISAMS northern hemisphere temperature on January 8, 1992, when planetary waves were strong in the mesosphere. Both measurements reveal consistent patterns of the planetary disturbance, but MLS wave amplitudes are significantly weaker than those observed by ISAMS. This is probably due to the poorer sensitivity and vertical resolution of the MLS temperature data at these altitudes.

These data remain as a research product, in need of further validation before they can be confidently used in scientific studies. One reason for this is that there exists a large discontinuity in the v5 temperature sensitivity across ~0.4 hPa, which can cause a problem in retrievals near this level. This discontinuity may not be evident in individual temperature profiles or averages. However, temperature perturbations can exhibit a sudden drop in amplitude, sometimes by as much as a factor of two, for pressures less than ~0.4 hPa. This discontinuity is intrinsic to the retrieval configuration that aims to merge two differently-resolved temperature measurements. Scientists wishing to use MLS temperature data above 0.46 hPa are strongly advised to consult the MLS science team before embarking on scientific studies.

S8. Geopotential Height

S9. Upper tropospheric humidity

S9.1. Changes from UTH v4.9 to v5

The most significant change between v4.9 and v5 UTH was the manner in which the wet and dry spectroscopic continua were estimated. V4.9 estimated these from the MLS radiances alone. The dry continuum was obtained by assuming that the smallest MLS radiances on a few selected days correspond to 0 %RHi. An appropriate pressure-squared function was fitted to the observed radiance profiles (allowing for the small contributions from minor species). The v4.9 wet continuum was similarly obtained, by assuming that the largest radiances corresponded to 100 %RHi, and
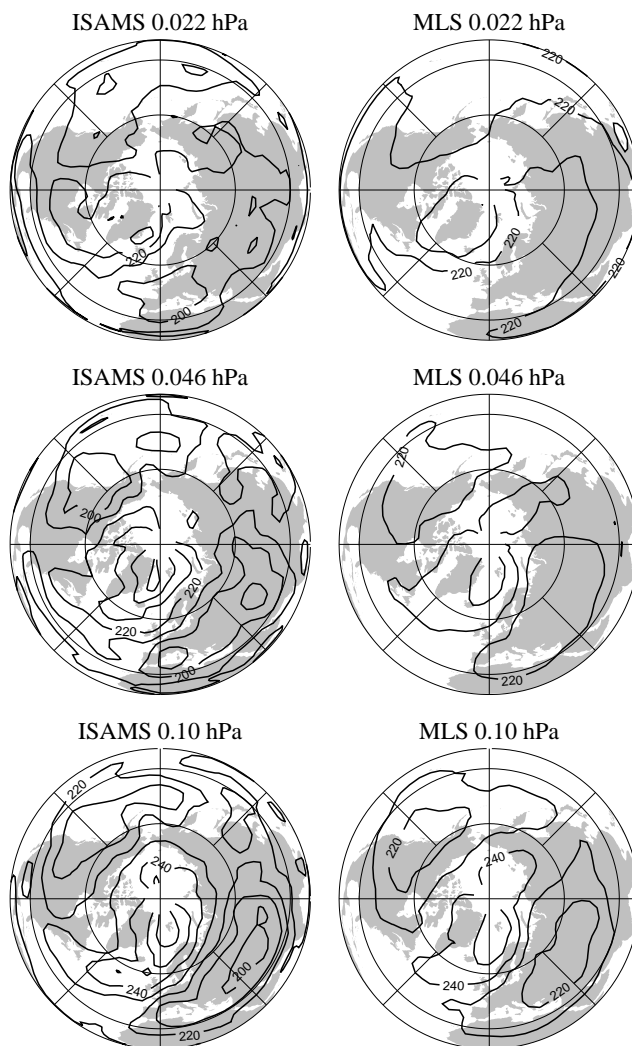

Figure S12. ISAMS and MLS mesospheric temperature on January 8, 1992. Contour intervals are 10 K, and latitude circles are shown at the equator, 30°N and 60°N.

Table S14. Characterization of MLS v5 mesospheric temperature.

Pressure / hPa	Vertical resolution[a] / km	Estimated precision[b] / K	MLS contribution[c] /K	v5−ISAMS /K
0.010	20	27	40	+9.7
0.015	20	26	44	+8.8
0.022	25	25	50	+7.1
0.032	25	24	55	+6.5
0.046	30	23	63	+5.5
0.068	20	22	57	+5.8
0.10	15	21	52	+3.4
0.15	10	19	48	+0.3
0.22	10	17	35	−0.4
0.32	10	15	29	+1.1

[a] As defined in section 6.2.
[b] Typical values given in Level 3AT files.
[c] See text.

fitting an appropriate continuum function (again, accounting for the minor species and dry continuum contributions). The temperature and tangent pressures used in these fits were from the MLS version 4 dataset.

In v5 the dry and wet continua were obtained simultaneously from a larger sample of selected profiles. As in v4.9, the dry continuum was obtained by assuming the smallest radiances corresponded to 0 %RHi. The v5 wet continuum, however, was obtained by using UTH profiles from coincident Vaisala radiosonde measurements. The MLS/sonde coincidence criteria applied for the fit were ±1°longitude, ±1°latitude, and ±3 hours. The v5 UTH data produced using these fitted continua agree with the Vaisala radiosondes within 5% on average between 300–150 hPa.

V5 has negative Level 3AT uncertainties where the estimated error is greater than 75 %RHi or the observed radiances are detected as being contaminated by cloud scattering. The v4.9 Level 3AT data give negative uncertainties only when a retrieval is not performed (the Level 2 UTH file simply reports that no retrieval was attempted). These situations arise when too few good tropospheric radiances are observed in a scan.

The time values given in the Level 2 UTH files differ between v4.9 and v5. The v4.9 files quote time in UT hours, while v5 uses UT milliseconds. Also, the v5 times are 32.786 s later than those in v4.9 (to be consistent with other MLS products).

The v5 H_2O files include data at pressures greater than 464 hPa; these should not be used in scientific investigations. The relative humidity at these levels is assumed to be the same as at 464 hPa.

S9.2. Estimated precision, accuracy, and resolution for v5 UTH

The estimates for v5 UTH precision, accuracy and resolution are given in Table S15. The basis for these values is the same as that for v4.9 [*Read et al.*, 2001]. Vertical resolution for 215 and 316-hPa levels are the full width at half maximum of the rows of the averaging kernel matrix, computed for the nominal MLS scan and radiance uncertainty. Outside the 464–147 hPa range, the forward model assumes constant relative humidity (constrained above to the 147 hPa and below to the 464 hPa values). This makes vertical resolution harder to define. We have chosen as a measure the distance between the lower (147 hPa) or upper (464 hPa) half maximum of the averaging kernel and the half maximum of the instrument weighting functions above (147 hPa) or below (464 hPa). The vertical resolution degrades with increasing moisture. The precisions in Table S15 account for the effects of radiance noise (0.1 K), tangent pressure precision (250 m), temperature uncertainty (2 K), and minor species corrections (0.4 ppmv for O_3, 1.5 ppbv for HNO_3, and 15 ppbv for N_2O) projected onto the UTH profile.

The accuracy estimate is based on the mean residual of the radiance fit to the dry and wet continuum functions, described above, propagated into UTH space. The uncertainties given in the UTH data files are estimates of accuracy, not precision. The unusual latitude-dependent artifact of 8 ppmv observed in the v4.9 dataset [*Read et al.*, 2001] is also observed in the v5 dataset. Therefore, any variability of a few ppmv seen in MLS UTH data may not reflect actual atmospheric conditions. As described in *Read et al.* [2001], care should be exercised when trying to 'join' the MLS UTH dataset to stratospheric H_2O observations (e.g., from MLS), especially where the 147 hPa level is in the stratosphere. The values in Table S15 only apply to v5 UTH for data taken before June 16, 1997.

Table S15. Estimated resolution, precision, and accuracy of MLS v5 UTH.

Pressure	Typical vertical resolution	Global		30°S–30°N		30°–60°(S and N)		60°–81°(S and N)	
/ hPa	/ km	Precision / %RHi	Accuracy / %RHi	Precision / %RHi	Accuracy / %RHi	Precision / %RHi	Accuracy / %RHi	Precision / %RHi	Accuracy / %RHi
147	3–4	24	26	37	39	11	11	30	27
215	3	11	25	17	23	5	24	21	33
316	3	9	25	7	23	10	24	14	38
464	3–6	20	52	22	64	26	50	21	45

S9.3. UTH after June 15, 1997

Table S16 shows the impact of the cessation of 63-GHz observations after June 1997, by comparing 'standard' data from earlier in the mission with data for the same days retrieved using the 'no 63-GHz' configuration.

The comparison shows significant differences between the two configurations, especially at high latitudes, and at 147 hPa globally. Since the 'standard' v5 data are a few %RHi drier than the v4.9 data, which are in turn mostly drier than correlative data [*Read et al.*, 2001], the post-June-1997 v5 product—being drier still—probably underestimates the true humidity. However, the scatter plots shown in Figure S13 indicate that the morphology of the data is reasonable, as the scatter is reasonably tight, compared to the precision of either dataset, except at 147 hPa. The large scatter at 147 hPa is due to the strong sensitivity at this level to the retrieved tangent pressure, which typically show differences between the two configurations equivalent to ~200 m.

S9.4. Caveats for v5 UTH data

The following caveats apply to the use of v5 MLS UTH data (note that these are different from those that apply to v4.9 data [*Read et al.*, 2001]). V5 data at 147 and 215 hPa should only be used where the corresponding uncertainty in the data file is positive. Any UTH values greater than 125 %RHi are indicative of the presence of clouds or supersaturation. In the absence of ancillary data to detect clouds, such values should be reset to 100 %RHi for a better estimate of the true humidity. Note that this threshold value applies only to the data taken before June 1997; an equivalent threshold for the post-June-1997 data remains to be determined.

The 147 and 215 hPa level are thought to be reliable when the UTH uncertainty is positive. The quality of UTH at 464 and 316 hPa is crucially dependent on the humidity above these levels. In cases where the atmosphere is very moist in the 215–147 hPa region, MLS will have little or no sensitivity to the water vapor lower down. As a first step in the UTH retrieval, a simple retrieval of mean humidity over 464–147 hPa is performed. The results of this 'initial guess' prove
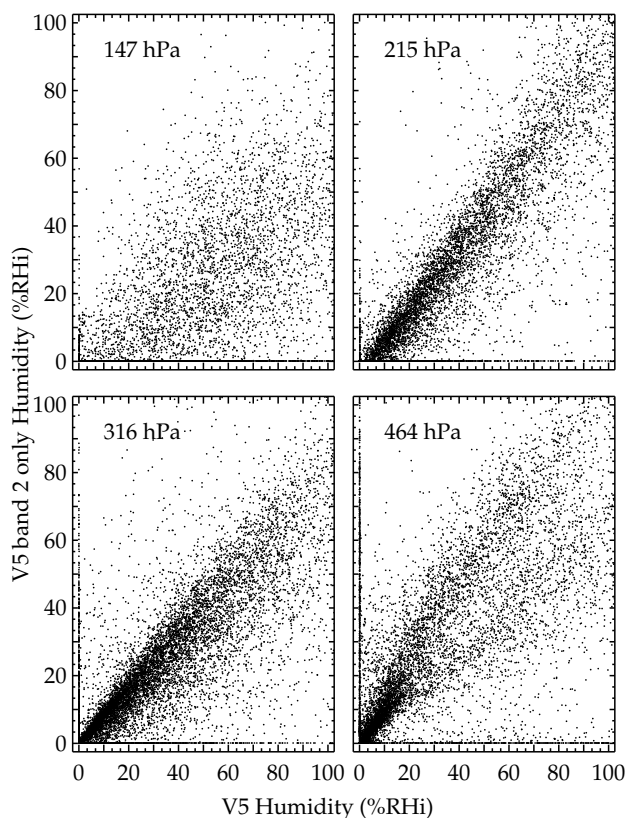

Figure S13. A comparison of UTH data taken over ten selected days given in section S6.1, processed with the 'standard' processing (x-axis) and the 'R2 only' mode (y-axis).

Table S16. Differences between '205-GHz only' and standard v5 UTH for several 1996 days.

Pressure	Global		30°S–30°N		30°–60°N		60°–81°N	
/ hPa	/ %RHi	/ %	/ %RHi	/ %	/ %RHi	/ %	/ %RHi	/ %
147	−23	−52	−56	−50	−4	−60	−9	−74
215	−4	−13	0	0	−6	−34	−6	−62
316	−7	−20	−4	−17	−7	−13	−14	−29
464	0	0	3	22	0	0	−7	−17

to be a useful indicator of moist situations. Study has shown that MLS UTH data at 316 and 464 hPa are reliable when their values are greater than the 'initial guess' (quoted in the Level 2 UTH file, as described in *Read et al.* [2001]) minus 5 %RHi, and the magnitude of their uncertainties (regardless of sign) is less than 110 %RHi. Even with this screen, data at the 464 and 316 hPa levels are expected to have a dry bias for humidities greater than 50 %RHi. However, information about the atmospheric morphology in these regions should still be useful. The Level 3AT UTH data files do not contain the information required to perform this screening. Therefore, we recommend the Level 2 UTH files be used in preference to the Level 3AT data.

Care should be taken when converting the MLS data from relative humidity to mixing ratio. As discussed in more detail in *Read et al.* [2001], the temperature data used for the conversion should be that planned for use in subsequent scientific analyses, rather than the NCEP/UARS climatology data used in the retrieval, as the latter could introduce biases.

S10. Ozone from 205-GHz Radiometer Data

MLS v4 differences with SAGE II coincident profiles are compared to the differences for v5 (during 1995–1996) in Figure S14. At pressures less than 1 hPa, percentage differences between the two datasets increase; this altitude range includes diurnal variability issues along the occultation ray path for SAGE II observations, so we are not surprised to see larger differences there. The total number of coincidences during 1995–1996 is about 650 for the high latitude bins and 1200 at low latitudes, but these numbers drop significantly for the lowest pressures reported for SAGE II data (0.1 hPa); also, the uncertainty for both measurements is larger at these pressures. However, these factors alone probably can not fully account for the observed 10 to 20% differences (or more) in average lower mesospheric profiles; these differences can change sign depending on whether SAGE II sunsets or sunrises are used, but no clear pattern emerges from the studies performed so far. We have illustrated in Figure S14 the MLS and SAGE II comparisons up to 0.22 hPa only, but we see no strong reason to degrade the MLS accuracy estimates for the lower mesosphere, compared to the
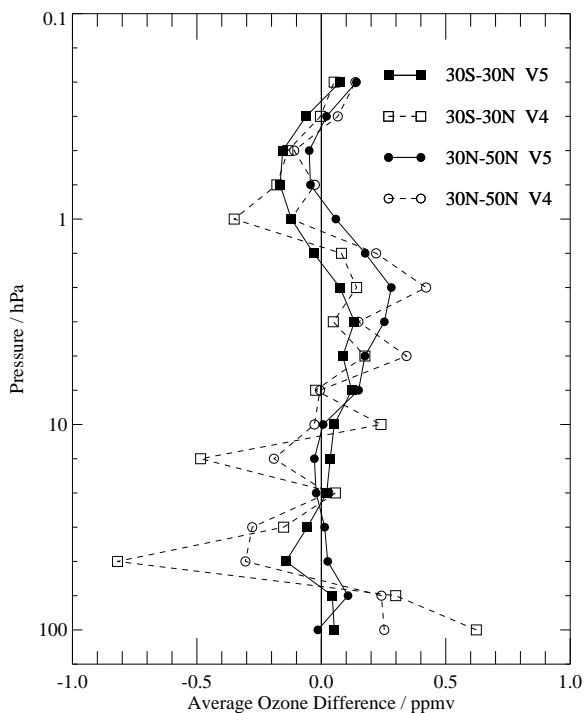

Figure S14. Average ozone differences (ppmv) for both MLS O3_205 v5 and v4 retrievals versus coincident SAGE II version 6.1 profiles over two latitude ranges (see legend) during the 1995-1996 time period. The discrepancies that occurred primarily because of poorer v4 MLS data quality in the lower stratosphere, especially at low latitudes, have been largely removed by using v5 MLS data. Abundance differences are calculated as MLS minus SAGE II values.
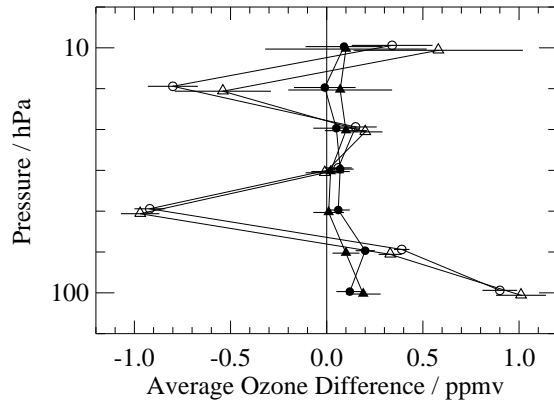
Figure S15. Average differences between MLS O3_205 retrievals and coincident ozonesonde profiles from the tropical sites Ascension Island (circles) and Brazzaville (triangles) for late 1991 and 1992; open symbols are for v4 and closed symbols are for v5. Differences are MLS minus ozonesonde values. There were 25 matching pairs of coincident profiles for Ascension Island and 24 for Brazzaville. Error bars give the standard errors for these average differences.

upper stratosphere. With sufficient averaging of the MLS profiles, there is probably useful information at pressures less than 0.22 hPa, but we conservatively use 0.22 hPa as an upper limit.

Figure S15 shows much smaller differences between MLS v5 and tropical ozonesonde averages (typically less than 0.1 ppmv for the average of about 25 total available coincidences for late 1991 through 1992) than for v4. Figure S16 shows good agreement between MLS v5 46 hPa data as a function of time and Ascension Island ozonesonde data (available during 1991 and 1992).

The mid-1998 to 1999 time period, when significant loss of data occurred because of scan slips, seems particularly affected in terms of data quality as well. Figure S17 shows that MLS zonal mean ozone data (shown for 30°S to 20°S) during this time period are noisier than in the preceding years for both lower (68 hPa) and upper (0.68 hPa) stratospheric levels. During this time period, the estimated ozone uncertainties show more extreme values (and scatter) as well. While these examples demonstrate some of the more obvious manifestations of poorer data quality because of the significant antenna scan slips during this time period, most other zonal means show smaller degradation.
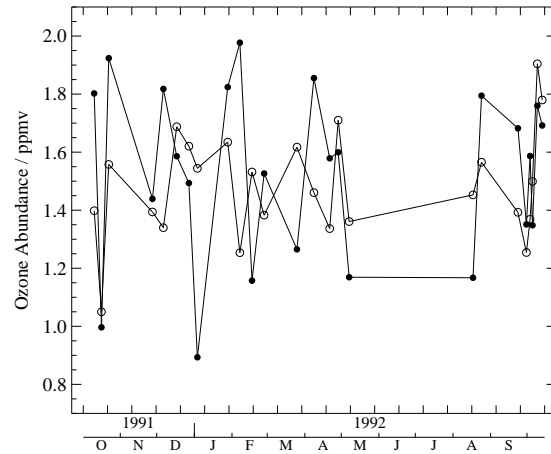
Figure S16. Time series comparison of 46 hPa ozone abundances from ozonesonde data (open circles) taken above Ascension Island in 1991 and 1992 with coincident (within 2°latitude, 12°longitude, same day) MLS v5 O3_205 values (dots). Estimated precision is about 0.25 ppmv for MLS values and better than 0.1 ppmv for the sonde data.

S11. Ozone from 183-GHz Radiometer Data

Figure S18 shows the three latest MLS versions of the O3_183 northern midlatitude mesospheric ozone diurnal cycle discussed for v3 by *Ricaud et al.* [1996]. For reference, Figure S18 also displays v5 O3_205, which is noisier than — but in ~10% agreement with — the mesospheric O3_183 data. *Ricaud et al.* [1996] also showed that ground-based microwave data on mesospheric ozone agreed with the MLS results in the lower mesosphere; ground-based microwave data from Table Mountain (California) were shown to exhibit better agreement with models than MLS data at 0.1 hPa, but somewhat poorer agreement at 0.04 hPa. These conclusions are consistent with the newer v5 MLS data for mesospheric O3_183.

S12. Stratospheric and mesospheric water vapor

Because version 104 is already validated and has been widely used, this section documents the differences between version 5 and version 104. Some of these differences are discussed in *Pumphrey et al.* [2000]. Note that the v104 data are available from the GSFC DAAC, where they are archived as 'version 6' MLS data.
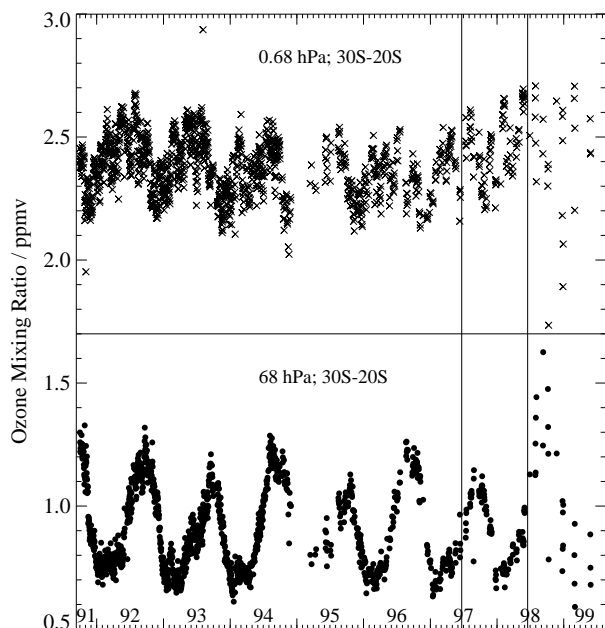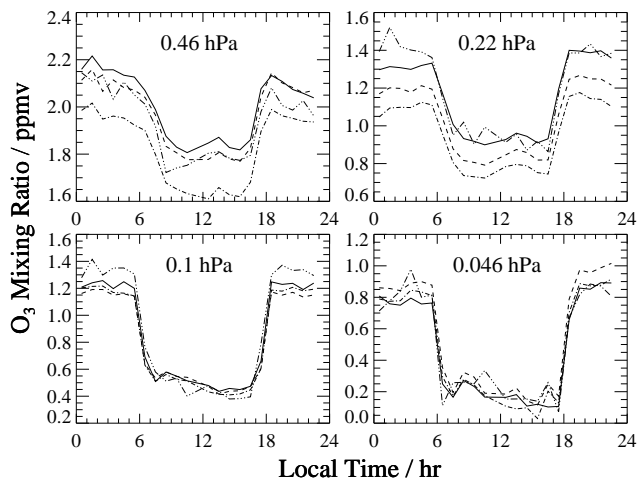
Figure S18. Comparison of the ozone diurnal variation at various mesospheric pressures for different MLS ozone retrieval versions: v5 O3_183 (solid lines), v4 O3_183 (dashed-dotted lines), v3 O3_183 (dashed lines), and v5 O3_205 (dashed-triple-dotted lines). These plots are for hourly averages and 40°N to 50°N zonal means for October 1991, the same conditions as for Figure 2 of *Ricaud et al.* [1996].

S12.1. Changes in algorithms for v5 H_2O

The relationship between H_2O mixing ratio and radiance is somewhat nonlinear, so an iterative retrieval is used, as described in section S4.3.3. In addition, the sideband ratios and the pressure broadening and shift parameters for the water vapor line were changed to values retrieved from the measured radiances [*Pumphrey and Bühler*, 2000].

S12.2. Differences between v5 and v104 H_2O.

Differences between MLS v5 and v104 H_2O are shown in Table S17. There is a significant break at 1 hPa – above this the two versions agree to within 0.1 ppmv up to 0.04 hPa while below it, version 5 is about 0.5 ppmv wetter.

S12.3. Estimated vertical resolution, precision and accuracy of v5 H_2O

Table S18 shows the estimated precision and accuracy of version 5 H_2O. The precision is calculated as in section 6 from the variability in an equatorial latitude bin, over four 5-day periods in the middle of UARS yaw months. (Variability within those 5-day periods is considered, not variability between them.) The column labeled "Ratio" has the meaning explained in section 6.

The accuracy is estimated by comparisons with other in-

Figure S17. Zonal mean time series of daily average ozone (205 GHz data) for 1991 through 1999 at 30°S to 20°S, for pressures of 68 hPa (dots) and 0.68 hPa (crosses). Vertical lines indicate the start of single radiometer mode in June 15, 1997, and the bad scan slip period on June 29, 1998.

Table S18. Estimated Vertical Resolution, Precision and Accuracy of MLS v5 H_2O.

Pressure / hPa	Vertical resolution[a] / km	Estimated precision / ppmv	/%	Precision ratio[b]	Estimated accuracy[c] / ppmv	/%
0.0100	8.4	0.39	19.3%	0.5	1.03	51.6%
0.0215	6.3	0.31	8.1%	0.5	1.02	26.8%
0.0464	6.1	0.23	4.5%	0.4	1.01	19.4%
0.100	5.7	0.26	4.9%	0.5	1.00	18.4%
0.147	7.5	0.18	3.2%	0.3	0.93	16.4%
0.215	5.3	0.22	3.9%	0.4	0.87	15.3%
0.316	7.0	0.18	3.1%	0.3	0.83	14.4%
0.464	3.5	0.18	3.1%	0.4	0.80	14.0%
0.681	3.7	0.19	3.3%	0.4	0.75	13.1%
1.00	4.3	0.20	3.5%	0.5	0.69	12.1%
1.47	3.7	0.20	3.5%	0.6	0.67	11.6%
2.15	3.3	0.16	3.2%	0.6	0.64	12.7%
3.16	3.2	0.15	3.1%	0.5	0.59	12.0%
4.64	3.1	0.14	3.2%	0.6	0.53	11.6%
6.81	3.1	0.14	3.0%	0.5	0.50	11.0%
10.0	3.1	0.13	2.9%	0.5	0.48	10.9%
14.7	3.2	0.12	3.0%	0.5	0.50	12.2%
21.5	3.4	0.15	3.7%	0.6	0.52	12.8%
31.6	3.4	0.16	3.6%	0.6	0.51	11.2%
46.4	3.7	0.17	4.0%	0.5	0.50	12.1%
68.1	5.3	0.28	7.5%	0.5	0.75	20.0%
100.	5.1	0.25	6.7%	0.2	1.00	27.0%

[a] As defined in section 6.2.

[b] Data file uncertainties should be multiplied by these numbers to obtain a better value for the '1σ' single profile precision (see text).

[c] Accuracies quoted here represent roughly a 95% confidence level ('2σ' values).

Table S17. Average Differences Between H_2O Data Versions

Pressure / hPa	v5−v104 / ppmv	v5−v104 / %
0.0100	+0.51	+29%
0.0215	+0.45	+12%
0.0464	+0.14	+2%
0.100	−0.09	−1%
0.147	−0.04	+0%
0.215	+0.01	+0%
0.316	+0.04	+0%
0.464	−0.01	+0%
0.681	−0.02	+0%
1.00	+0.08	+1%
1.47	+0.36	+6%
2.15	+0.22	+4%
3.16	+0.45	+9%
4.64	+0.33	+7%
6.81	+0.60	+13%
10.0	+0.50	+12%
14.7	+0.34	+8%
21.5	+0.30	+7%
31.6	+0.68	+16%
46.4	+0.35	+8%
68.1	+0.44	+12%
100	+0.23	+6%

struments, including HALOE (HALogen Occultation Experiment) and ATMOS (Atmospheric Trace Molecule Spectroscopy Experiment), as described below, and also the ground-based microwave instrument WVMS (Water Vapor Millimeter-wave Spectrometer) [*Nedoluha et al.*, 1997] and a balloon-mounted frost-point hygrometer (FPH). Comparisons of version 104 with FPH and WVMS are described in [*Pumphrey*, 1999] – the comparisons done here for v5 were carried out in the same manner and were consistent with the HALOE and ATMOS comparisons described below.

The version 5 data in the lower stratosphere contain two types of systematic error which vary on a timescale of days to weeks. The timing of these artifacts coincides with the UARS yaw cycle and with the ends of calendar months. The first of these effects is caused by changes in the antenna temperature while the second is caused by the a priori, which changes from one calendar month to the next. These effects are illustrated in figure S19.

S12.4. Correlative comparisons for v5 H_2O

In this section we compare MLS data to data from two solar occultation instruments: HALOE [*Harries et al.*, 1996] and ATMOS [*Gunson et al.*, 1996]. For each profile used from each of these data sets the difference was taken with
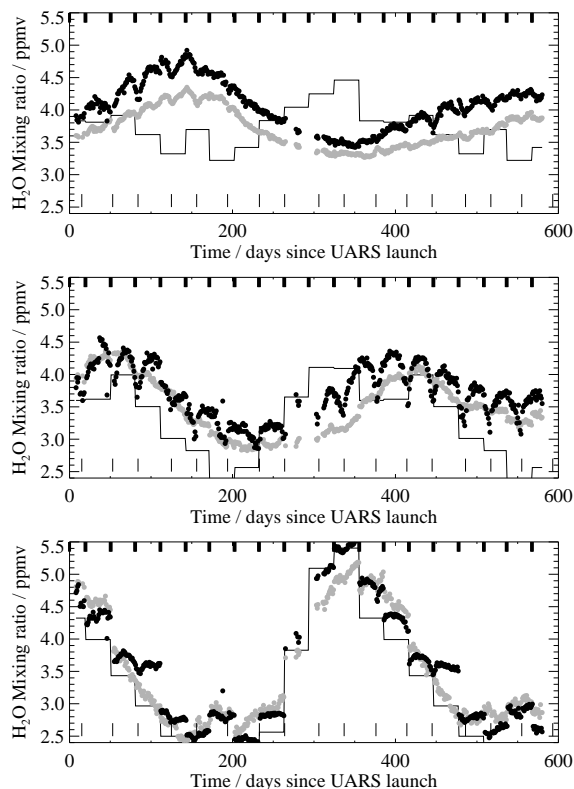
the closest MLS profile for the same day. The two profiles are typically separated by less than $15°$ in longitude and $2°$ in latitude. The difference was averaged over a number of pairs of profiles to yield a mean difference, which gives an indication of the systematic bias between the two instruments. This is shown in figures S20 and S21 as a solid line. We also calculated a root-mean-square (rms) difference which is shown in figures S20 and S21 as a dotted line. This will equal the absolute value of the mean difference if all of the difference is systematic and exceed it if some of the difference is random. To aid this comparison where the mean difference is negative, the absolute mean difference is shown in the figures as a dashed line. The rms difference should be of a similar size to the root-sum-square combined uncertainties of the two measurements, which is shown in the figures as a dot-dash line.

S12.4.1. HALOE This comparison uses every HALOE profile for which a co-located MLS profile is available. The results are shown in Figure S20. The MLS v5 profile is drier than HALOE in the mesosphere, but wetter than it in the stratosphere. This behavior contrasts somewhat with v104, which is uniformly drier than HALOE. On the whole, the differences between the two instruments are within the quoted errors (the dotted line in Figure S20 is inside the dot-dash line). In the mesosphere the difference is much smaller than the quoted errors: this is because the error bars supplied with the HALOE data are very large.

S12.4.2. ATMOS ATMOS is a solar occultation instrument which flew on several space shuttle missions of which two occurred during the operational life of the MLS 183-GHz radiometer. We have collected all the profiles from these two missions for which a coincident MLS profile exists and carried out a comparison as described above. The results are shown in Figure S21. The ATMOS data used were version 3, described in *Michelsen et al.* [2002].

MLS v5 agrees well with ATMOS in the stratosphere but is considerably drier in the mesosphere. The similarity between Figures S20 and S21 suggests that the bias in MLS v5 H_2O changes rapidly with altitude near 1 hPa. MLS v104, on the other hand, has a fairly uniform dry bias throughout the stratosphere and lower mesosphere.

In the light of these comparisons and the systematic errors discussed in section S12.3 we recommend v104 H_2O be used in preference to v5, especially in the lower stratosphere, taking note of the v104 dry bias of 0.2-0.5 ppmv. In the mesosphere, there is little difference between v104 and v5.
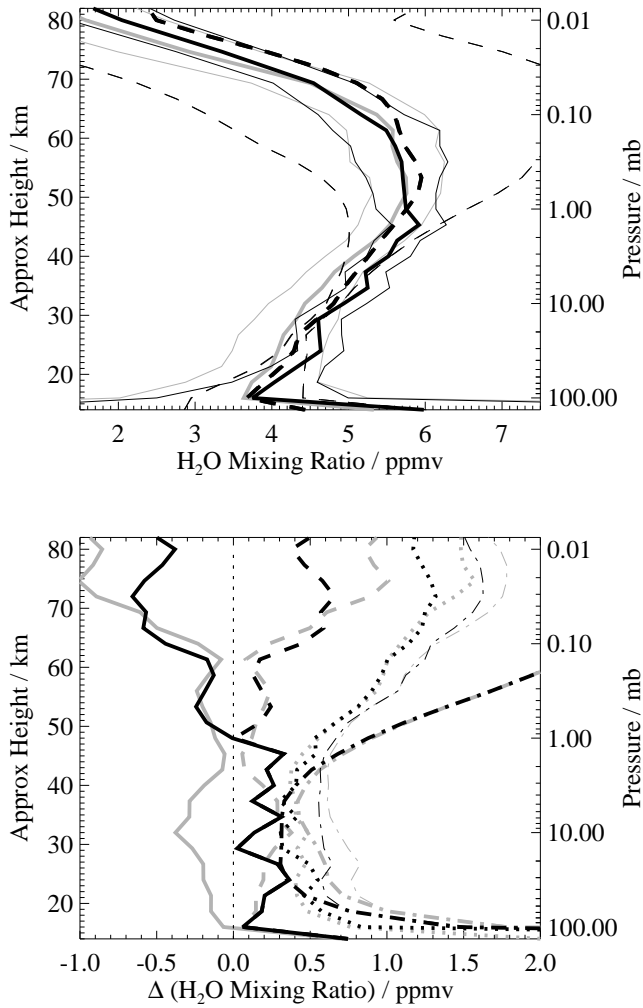

Figure S19. Time series of equatorial MLS H_2O, at 100 hPa (bottom), 68 hPa (middle) and 46 hPa (top). The black dots are version 5, the grey dots are version 104. The thin line is the a priori used for both versions. The ticks near the bottom of each panel mark the UARS yaws; the ticks near the top of each panel mark calendar month boundaries.

Figure S20. Comparison of MLS and HALOE H_2O. Top panel: mean profiles of MLS v5 (solid) and HALOE v19 (dashed). MLS v104 is shown in grey for comparison. Thin lines are error bars for the thick lines of the same color and dash pattern. Bottom panel: Solid lines show differences between MLS and HALOE v19; dashed lines are the absolute value of this difference. Black lines are MLS v5 and grey are MLS v104. The dotted line is the rms difference between MLS and HALOE and the dot-dash line is the rss of the quoted errors of the two instruments. (The thin dot-dash line is the same as the thick one except that the standard deviation of the HALOE data is used in place of the quoted errors which seem unduly pessimistic in the mesosphere.)
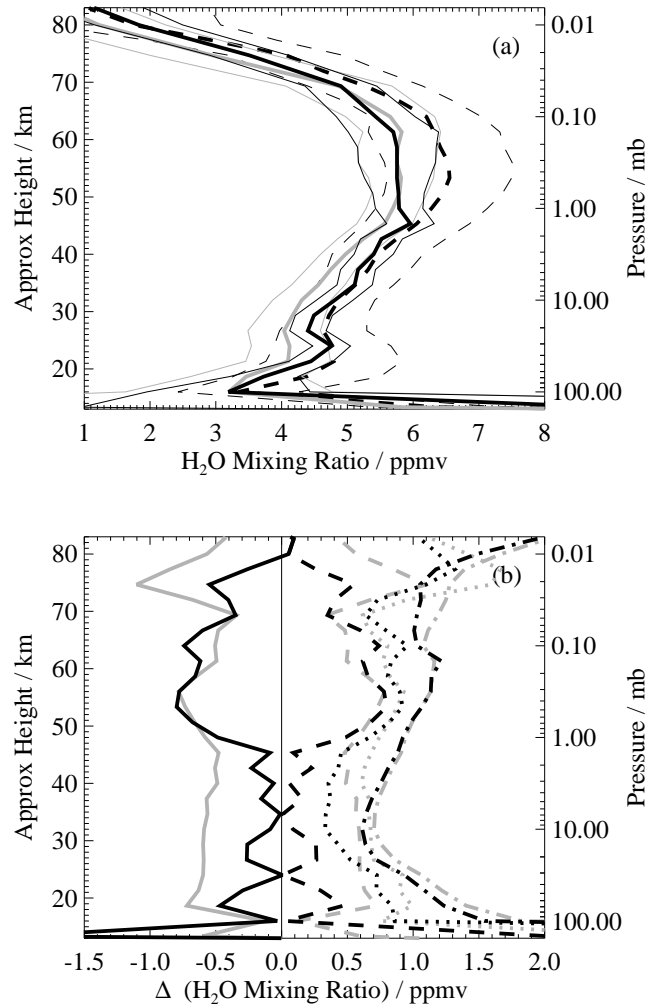
Figure S21. As Figure S20 but for MLS and ATMOS H_2O.

S13. Chlorine Monoxide (ClO)

Several papers published since *Waters et al.* [1996] have further attested the general validity of MLS ClO. *Feist et al.* [2000] found that Millimeter-wave Atmospheric Sounder (MAS) 'day' minus 'night' ClO measurement agreement with MLS is typically better than 0.1 ppbv in the tropical and midlatitude regions where the two instruments have coincident measurements. *Khosravi et al.* [1998] found that MLS ClO measurements agree well with model results in the upper stratosphere when the model methane is constrained by HALOE measurements and a 6% $HCl+O_2$ channel for the ClO+OH reaction is included per laboratory measurements of *Lipson et al.* [1997]. *Ricaud et al.* [2000] found that the MLS ClO diurnal variations in the middle and upper stratosphere agree with model calculations to within 5–10%, and that seasonal variations imply an evolution essentially dictated by the variation in partitioning with HCl, together with partitioning within the ClO_x family above 40 km. The differences found above 50 km are attributable to uncertainties in reaction rates. The analyses of *Froidevaux et al.* [2000] show that the increase in MLS upper stratospheric ClO during 1992–1995 is larger than expected from CFC increases, and is consistent with implications from the decline in CH_4 observed by HALOE during this period as found by *Siskind et al.* [1998]. *Froidevaux et al.* [2000] further show that the decrease in lower stratospheric ClO observed by MLS during 1991–1997 is consistent with relaxation from chemical perturbation induced by the Pinatubo volcanic eruption. *Massie et al.* [2000] show that the variation of five-day averages of MLS lower stratospheric ClO are consistent with heterogeneous model calculations for the 1995–1996 Arctic early winter. *Waters et al.* [1999] summarize results of additional analyses of the MLS ClO data.

S13.1. Changes in algorithms for v5 ClO

The algorithm for setting QUALITY_ClO to '4' (indicating good radiances and retrievals) has been changed in v5 because of changes in the v5 radiance-fit chi-square statistic, which is not as highly correlated with 'spikes' in retrieved ClO as in v4 or v3. This algorithm was determined empirically by choosing chi-square criteria (including bands 2, 3 and 4) that eliminate most unreasonable 'spikes' while not throwing out an excessive amount of good data. With the exception of a few months when unusual instrument or satellite problems occurred, the general criteria for selecting good ClO retrievals (QUALITY_CLO='4', MMAF_STAT = 'G', 'T' or 't') discard ~3% of all v5 data compared to ~1.5% for v4. For records with MMAF_STAT = 'G', 'T' or 't' (the same in v5 and v4), more records in v5 (~2%) are assigned quality flags less than '4' than in v4 (~0.2%).

As in v4, retrievals of HNO_3 are done in v5 that reduce or eliminate the HNO_3-caused bias in enhanced polar lower stratospheric v3 ClO as described by *Waters et al.* [1996]. Also, as in v3 and v4, a linear forward model is used in the v5 ClO retrievals; thus the ~10% scaling uncertainty due to lack of radiance 'closure' described in *Waters et al.* [1996] is not expected to be significantly reduced in v5, although the v5 retrievals on every surface may have reduced it somewhat. The algorithms do not force retrieved ClO values to be positive; doing so would cause positive bias artifacts in averages made from individual profiles. Individual retrieved values will often be negative because of instrument noise. (Note that this is a different issue than the reduction of negative values in *averages* of nighttime ClO data, mentioned in the main portion of this paper, due to retrieval of CH_3CN in v5.)

S13.2. Determining biases in lower stratospheric ClO data

Limitations of the data processing algorithms to account for curvature and features in the observed limb spectra with an accuracy better than ~0.1 K brightness introduce a (thought to be mostly 'bias') uncertainty of ~0.1 ppbv in retrieved ClO. This uncertainty is believed less severe in the upper stratosphere than in the lower where there are more spectral features and the broader lines make measurement of 'baseline' more difficult. However, a robust feature of models that predict diurnal behavior of ClO [*Ko and Sze*, 1984; *Froidevaux et al.*, 1985; *Ricaud et al.*, 2000, for example] is that — at heights below ~35 km (pressures above ~5 hPa) and away from enhanced chlorine chemistry in the winter polar vortices — the ClO abundances at night decrease essentially to zero. Very accurate *in situ* measurements of midlatitude ClO at 20 km show nighttime abundances of no more than the detection threshold of ~0.001 ppbv, in agreement with the model predictions [*Brune et al.*, 1990]. By assuming that nighttime lower stratospheric ClO abundances are zero away from the winter polar vortices, we can infer biases in the MLS ClO data.

Figure S22 shows the time-series of monthly average v5 nighttime ClO on each retrieval surface between 6.8 hPa and 100 hPa for the first ~3 years of the UARS mission in which MLS operations were mostly normal. The nighttime values were selected for local solar time between midnight and 6 a.m. (to avoid including evening measurements when ClO can still be decaying from daytime values) and for solar zenith angles greater than 90° (to avoid including measurements where sunrise occurs before 6 a.m.). The points in Figure S22 generally lie in a tight cluster at each level (other than 100 hPa) with relatively few outside the cluster. The two 60°N–80°N points at 6.8 hPa in late February 1992 and
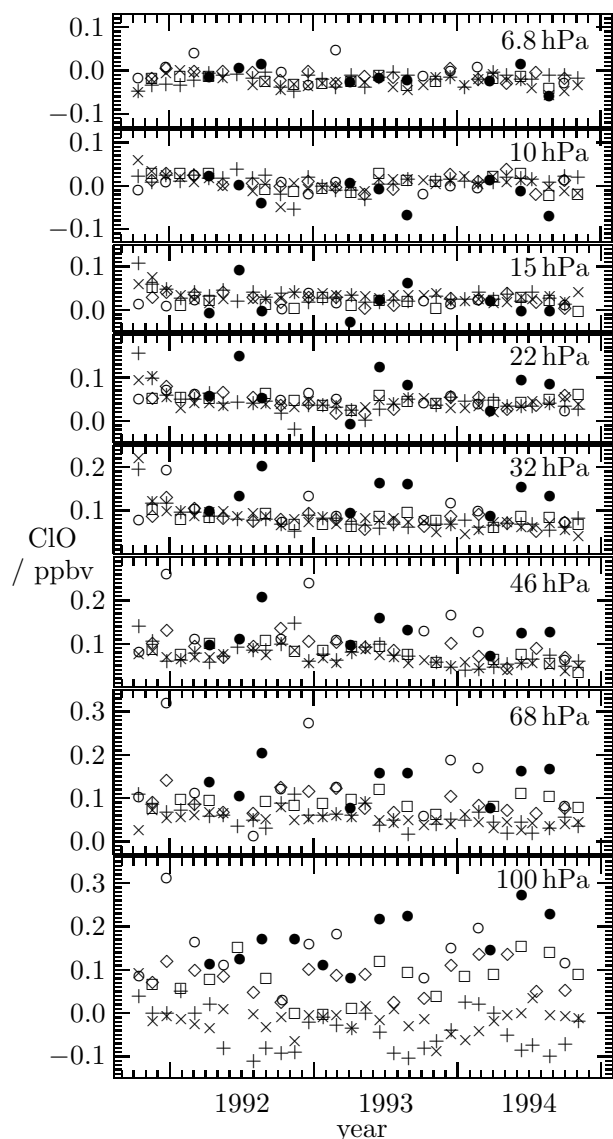
Figure S22. Time series of v5 ClO monthly zonal means for measurements between midnight and 6 a.m., and solar zenith angles greater than 90°: 60°N–80°N(○), 30°N–60°N(◇), 0°–30°N(+), 0°–30°S(×), 30°S–60°S(□), 60°S–80°S(●). Each point is the average for one UARS month. A point is included only if there are >300 individual retrievals meeting the standard quality criteria, corresponding to expected precision due to instrument noise of better than ∼0.02 ppbv (∼0.04 ppbv at 100 hPa). Typically, 1000–4000 individual profiles were used in each average, corresponding to better than ∼0.01 ppbv expected precision. Small ticks on the horizontal axis are calendar month boundaries.

1993 are where examination of the profiles indicate that de-

scent of more abundant ClO from higher altitudes reached 6.8 hPa. The larger 0°–30°N and 0°–30°S values in October 1991 at 15, 22, and 32 hPa can be explained by residual effects of Pinatubo SO_2 not accounted for in v5. The 60°N–80°N and 60°S–80°S points lying above the general cluster all occur during winter, and are thought due to increased nighttime ClO from thermal decomposition of enhanced ClOOCl. MLS ClO maps for January 1992 show enhanced nighttime ClO in warmer regions of the Arctic vortex with abundances that are consistent with the amounts expected for thermal decomposition of ClOOCl [*Waters et al.*, 1993]. Examination of the nighttime ClO abundances for the Antarctic and Arctic winter vortices given in Figures 8 and 9 show that they vary with temperature and pressure in reasonable agreement with predictions for ClOOCl thermal decomposition provided by R.J. Salawitch [private communication]. The ∼ −0.05 ppbv 60°S–80°S values at 10 hPa in August 1992, 1993 and 1994 that stand out from the cluster are unexplained, and probably — since they all occur at the same month in each of the three years — represent some atmospheric effect that is not accounted for in the retrievals. Nothing unusual occurred in MLS operations during these months that is thought to affect the ClO, nor that would cause the 'abnormal' values (differing by ∼0.05 ppbv from the cluster) at 0°–30°N and 0°–30°S 10 hPa in Oct–Nov 1992, at 60°S–80°S 15 hPa in April 1993, and at 0°–30°N 22 hPa in November 1992 — so these observations may indicate some unexplained atmospheric effect. The scatter in the points at 100 hPa, and to a much lesser extent at 68 hPa, is significantly larger than can be explained by instrument noise and varies with latitude. This is likely to be due to some unaccounted atmospheric phenomenon that is affecting the radiances, and thus retrievals, at these low altitudes.

Figure S23 shows — for altitudes where nighttime ClO is thought to be 'zero' — the profile of retrieved nighttime ClO averaged over 60°S–60°N for three portions of the UARS mission as indicated in the caption. We interpret the curves in Figure S23 as bias artifacts in MLS v5 ClO.

S14. Nitric Acid

We use Equation (S5), with all radiances collapsed into one vector and the a priori term neglected, to formulate a 'corrected' HNO_3 retrieval, $\mathbf{x}'$, that accounts for the contributions from the ν_9 and ν_7 excited vibrational states:

$$\mathbf{x}' = \mathbf{x} + \left[\mathbf{S_a}^{-1} + \mathbf{K}'^{\mathrm{T}} \mathbf{S_y}^{-1} \mathbf{K}' \right]^{-1}$$
$$\left(\mathbf{K}'^{\mathrm{T}} \mathbf{S_y}^{-1} \left[\mathbf{y} - \mathbf{f}'(\mathbf{x}) \right] \right)$$

where $\mathbf{K}'$ is an improved weighting function matrix ($\mathbf{K}' = \mathbf{K} + \mathbf{k}$) that includes the contributions from the ground state,
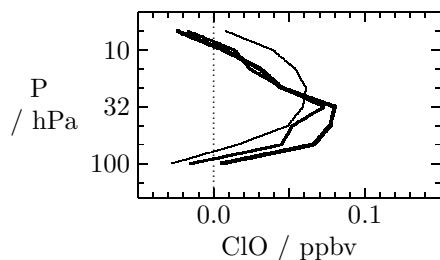
Figure S23. Bias in MLS v5 ClO determined from average of nighttime (0–6 a.m., sza>90°) retrievals between 60°S and 60°N. Thick line: average of 323,630 individual retrieved profiles from measurements taken between October 1, 1991 and November 19, 1994, when MLS operations were mostly normal. Medium line: average of 70,454 profiles between February 1, 1995, and June 15, 1997, in which antenna scan slips occurred. Thin line: average of 33,136 profiles between June 15, 1997, and March 30, 2000, when only the 205-GHz radiometer was operated and scan slips also occurred. The expected precison, based on instrument noise, varies from <0.001 ppbv for the thick line to ~0.002 ppbv for the thin line.

K, and the excited vibrational states, **k**. Similarly, a corrected forward model is defined to be the original v5 forward model plus the extra terms from the excited vibrational states: $\mathbf{f}'(\mathbf{x}) = \mathbf{f}(\mathbf{x}) + \mathbf{k}\mathbf{x}$. Assuming that the retrieval, based on the flawed forward model $\mathbf{f}(\mathbf{x})$, fits the radiances optimally (i.e., zero mean radiance residual), then in the mean $\mathbf{y} - \mathbf{f}(\mathbf{x}) = 0$. Substituting in for $\mathbf{f}'(\mathbf{x})$, defining a new solution covariance, $\mathbf{S}'_{\mathbf{x}}$, similar in form to that in Equation (S6), and rearranging leads to:

$$\mathbf{x}' = \mathbf{x} + \mathbf{S}'_{\mathbf{x}}\mathbf{K}'^{\mathrm{T}}\mathbf{S}_{\mathbf{y}}^{-1}\left[-\mathbf{k}\mathbf{x}\right]$$
$$= \mathbf{C}(\mathbf{T})\mathbf{x}. \qquad (S42)$$

Thus the correction is a linear scaling of the original profile. The correction matrix, $\mathbf{C}(\mathbf{T})$, is temperature dependent because of the strong temperature dependence of the HNO_3 excited vibrational states. $\mathbf{C}(\mathbf{T})$ is nearly tridiagonal and is assumed to be so in order to derive an easily-implemented empirical correction. The full model was run for eight representative temperature profiles spanning the variations that occur in stratospheric temperatures for different seasons and latitudes. The selected temperature profiles are shown in Figure S24. $\mathbf{C}(\mathbf{T})$ was computed for each case, and the eight results for each tridiagonal element were combined and fitted with a simple linear polynomial in temperature. The tridiagonal elements of the correction matrix are thus rep-
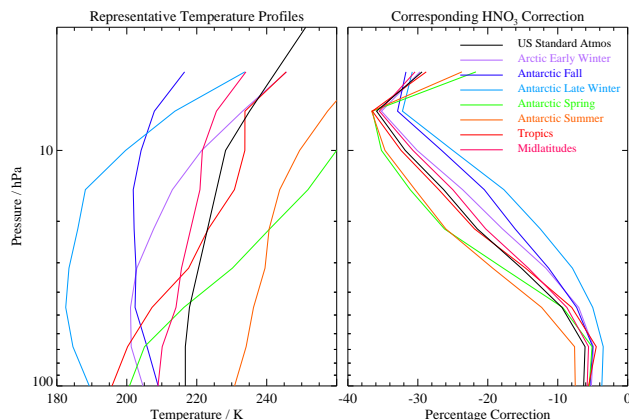

Figure S24. Temperature profiles used to derive the empirical correction to the MLS v5 HNO_3 data (left) and the associated percentage changes in HNO_3 mixing ratio (right).

resented by:

$$C_{l-1,l}(T_{l-1}, T_l) = \alpha_{l-1,l} + \beta_{l-1,l}T_{l-1} + \gamma_{l-1,l}T_l,$$
$$C_{l,l}(T_l, T_l) = \alpha_{l,l} + \beta_{l,l}T_l, \qquad (S43)$$
$$C_{l,l+1}(T_l, T_{l+1}) = \alpha_{l,l+1} + \beta_{l,l+1}T_l + \gamma_{l,l+1}T_{l+1},$$

where α, β and γ are the coefficients of a linear polynomial in temperature, T is the atmospheric temperature, and l denotes a particular altitude level in the HNO_3 profile. The coefficients α, β and γ for the diagonal and the two adjacent sets of elements are provided in Table S19. This polynomial correction is valid over the height range 100 to 4.6 hPa and provides an estimated rms accuracy of 0.2 ppbv for corrected HNO_3 throughout the domain. The corresponding reductions in the reported v5 HNO_3 mixing ratios for the eight representative cases are shown in Figure S24.

The tabulated coefficients can be used along with an associated temperature profile (either from MLS or from some meteorological analyses interpolated to the MLS measurement location) to correct each HNO_3 profile in the MLS dataset. Because this correction leads to increases in the values of the weighting function matrix, it also produces a smaller error covariance. Thus it is necessary to correct not only the mixing ratios, but also the associated uncertainty values given in the Level 3AT files. Although the uncertainty values change with altitude, they are fairly constant over both latitude and time (over the course of the UARS mission), so the correction for them is simpler than for the highly variable mixing ratios. Tests comparing the elements of $\mathbf{S}'_{\mathbf{x}}$ and $\mathbf{S}_{\mathbf{x}}$ (i.e., the original v5 solution covariance) indicate that the uncertainty values are changed negligibly at 100, 68, and 46 hPa, but the values reported in the Level 3AT

files should be decreased by 0.1 ppbv at 32 and 22 hPa, by 0.2 ppbv at 15 and 10 hPa, and by 0.3 ppbv at 6.8 and 4.6 hPa.

S15. Methyl Cyanide

No supplementary material.

S16. Summary and conclusions

S16.1. Lessons learned from version 5

This paper describes the v5 algorithms as implemented and the data they produced. The work has also identified issues that may have benefited from more study during the development and configuration of the v5 software. The most notable of these are the issues associated with the use of off-diagonal terms in the a priori covariance matrices (see section S3.2) and their impact on the observed scatter in the data, described in section 6.1. In retrospect, the length scales chosen for O_3, H_2O, HNO_3 and CH_3CN were probably longer than optimum. Another issue that may have warranted more investigation during the development of the v5 algorithms is the trade-off between the baseline and extinction elements of the state vector, described in section S3.6. The retrieval algorithms typically retrieved larger baseline terms than one might expect, using negative values for the extinction factor to compensate. More detailed study of the constraint of these terms may have lessened this rather inelegant effect. However, this issue had negligible impact on the main MLS data products.

There are no plans to perform further reprocessing on the UARS MLS dataset. However, the lessons learned from v5 are being applied to the algorithms and software for EOS MLS, planned for launch on the EOS Aura platform in 2004.

S17. MLS operations and data coverage

Table S20 gives a chronology of MLS operations and events that significantly impacted data collection or quality. Figure S25 gives a calendar of daily data coverage from launch through the end of 1999.

UARS was launched on September 12, 1991, and the first full day of MLS data was obtained on September 21. During late September and October 1991, time was spent characterizing the MLS performance and 'tuning' its operations. On October 31, a limb scan was implemented with denser vertical spacing of measurements in the lower stratosphere than at other altitudes; this scan pattern has been used in normal operations for the remainder of the mission.

Problems with the UARS solar array caused MLS, or portions of it, to be turned off during much of the early southern winter observing period in June 1992. In late 1992, low

voltage from the UARS power supply at spacecraft sunrise started affecting the MLS switching mirror movement during a few limb scans each orbit and caused excess noise in the measurements—most notably in ClO, as evidenced by the increased χ^2-statistic for ClO (see Figure 1 of *Waters et al.* [1996]). The switching mirror was not moved during a few limb scans under spacecraft sunrise low voltage conditions from November 18, 1992 until August 9, 1993, when the low voltage problem was circumvented with a solution using the secondary commutator of the switching mirror motor.

In late 1992 the 183-GHz radiometer started showing increased noise, which eventually developed into erratic behavior. The last full day of useful 183-GHz measurements (stratospheric H_2O and 183-GHz O_3) was April 15, 1993. This radiometer was turned off on April 24, 1993 after analyses indicated failure of its mixer.

The MLS antenna scanning mechanism began exhibiting signs of wear by early 1994; the period from March to July 1994 was primarily devoted to testing new operational modes, resulting in significantly reduced data. Continuing difficulties with the MLS scan system, and with the UARS batteries and solar array, caused severely limited data collection from October 1994 through July 1995. Various modifications to the operation of the antenna scanning mechanism were implemented in February 1995, and in June 1995 a schedule of (typically) 2 days of scanning followed by 1 day of 'rest' was adopted to conserve lifetime. During some of the period after March 1994, MLS was operated in a 'limb-tracking' mode to provide data on atmospheric gravity wave activity [*Wu and Waters*, 1996] while not causing excessive wear on the scan mechanism.

The UARS solar array, because of problems with its drive systems, was 'parked' in May 1995, resulting in a decrease of available power and an instrument power sharing mode with MLS periodically turned off. The UARS onboard computer experienced an anomalous shutdown in May 1997, stressing the batteries and leading to one (of three) being removed from service. Because of the degrading UARS power situation, MLS made measurements on only 6 days during May and June 1997. The 63-GHz radiometer that provided tangent pressure and temperature was turned off after June 14, 1997 to save power. MLS was put in 'standby mode' in July 1999 to conserve its remaining lifetime for possible overlapping measurements with the MLS to be launched on the EOS Aura mission in 2003. It was operated again for two brief periods in February and March 2000 to obtain Arctic observations [*Santee et al.*, 2000], and briefly in mid-August 2001 to obtain correlative observations for the Odin satellite.

Table S19. Correction coefficients for computing $C_{l-1,l}(T_{l-1}, T_l)$, $C_{l,l}(T_l)$, and $C_{l,l+1}(T_l, T_{l+1})$

Pressure / hPa	$\alpha_{l-1,l}$	$\beta_{l-1,l}$	$\gamma_{l-1,l}$	$\alpha_{l,l}$	$\beta_{l,l}$	$\alpha_{l,l+1}$	$\beta_{l,l+1}$	$\gamma_{l,l+1}$
4.6	−0.013	-1.0×10^{-5}	-2.2×10^{-4}	1.009	-5.0×10^{-4}	—	—	—
6.8	−0.007	-5.0×10^{-5}	-2.5×10^{-4}	1.036	-7.2×10^{-4}	−0.009	-5.0×10^{-5}	-2.5×10^{-4}
10	0.014	-1.2×10^{-4}	-3.1×10^{-4}	1.097	-1.07×10^{-3}	0.013	-1.2×10^{-4}	-3.1×10^{-4}
15	0.055	-2.8×10^{-4}	-3.3×10^{-4}	1.168	-1.40×10^{-3}	0.054	-2.8×10^{-4}	-3.3×10^{-4}
22	0.081	-2.2×10^{-4}	-4.4×10^{-4}	1.220	-1.57×10^{-3}	0.081	-2.2×10^{-4}	-4.4×10^{-4}
31	0.066	-2.2×10^{-4}	-2.8×10^{-4}	1.198	-1.35×10^{-3}	0.066	-2.2×10^{-4}	-2.8×10^{-4}
46	0.034	-2.2×10^{-4}	-5.0×10^{-5}	1.158	-1.05×10^{-3}	0.035	-2.2×10^{-4}	-5.0×10^{-5}
68	0.013	-1.3×10^{-4}	1.0×10^{-5}	1.117	-7.6×10^{-4}	0.013	-1.3×10^{-4}	1.0×10^{-5}
100	—	—	—	1.084	-5.4×10^{-4}	0.006	-7.0×10^{-5}	1.0×10^{-5}

Table S20. Chronology of significant events relevant to UARS MLS operations and data.

| Calendar day(s)	UARS day number(s)	Event
Sep 12, 1991	1	UARS launch
Sep 18, 1991	7	All MLS systems and subsystems on
Sep 21, 1991	10	First full day of MLS atmospheric data
Sep 23, 1991 – Oct 1, 1991	16-20	MLS initial characterization period, UARS roll-up on Sep 30
Oct 17–30, 1991	36–49	Some 'tuning' of MLS operations
Oct 31, 1991	50	Started using limb scan with denser sampling in lower stratosphere
Nov 1–2, 1991	51-52	UARS in safehold mode
Mar 17, 1992	188	UARS instruments inadvertently off at 10:36 UT; MLS back at 19:00 UT
Apr 8, 1992	210	MLS oblateness correction resolution changed from 2.5 to 1.25 km
Jun 2, 1992	265	UARS solar array drive anomaly; instruments turned off at 19:42 UT
Jun 14, 1992	277	MLS back on and fully operational
Jun 19 – Jul 9, 1992	282–302	183-GHz radiometer (and band 3 of 205-GHz) off to reduce power
Jul 14–17, 1992	307–310	MLS off; back on at 17:00 UT on 17 Jul
Oct 11, 1992	396	MLS moon scan for field-of-view calibration
Nov 18, 1992	434	Stopped moving switching mirror when voltage low at UARS sunrise
Mar 15, 1993	551	All UARS instruments off at 13:57 UT; MLS back operational at 22:45
Apr 6, 1993	573	UARS roll maneuver; nominal operations resumed at 05:00 UT
Apr 15, 1993	582	Last full day of data from 183-GHz radiometer
Apr 16–20, 1993	583–587	UARS in safehold mode; MLS scan stopped
Apr 24, 1993	591	183 GHz radiometer turned off, following failure of its mixer
Aug 9, 1993	698	Resumed moving switching mirror at sunrise via secondary commutator
Sep 18 – Oct 21, 1993	738–771	No limb scans much of this time because of UARS solar array problem
Dec 23, 1993 – Jan 25, 1994	834–867	Initial period of MLS scan slips
Jan 26, 1994	868	Start limb scanning in reverse (upward) direction: more motor torque
Jan 28 – Feb 4, 1994	870–877	MLS in safehold
Mar 1, 1994 – May 23, 1994	902–985	Reduced days of limb scans to conserve scan mechanism lifetime
Jul 5, 1994 – Aug 4, 1994	1028–1058	Limb scans on alternate days to conserve scan mechanism lifetime
Sep 19, 1994 – Oct 20, 1994	1104–1135	Limb scans on alternate days to conserve scan mechanism lifetime
Sep 23, 1994	1108	MLS moon scan for field-of-view calibration
Oct 1, 1994 – Jun 13, 1997	1116–2102	Intermittent limb scans during this period
Jun 14, 1997	2103	63 GHz radiometer turned off to reduce power drain on UARS
Jun 15, 1997 – 27 Jul 1999	2104–2876	Only occasional limb scans; MLS off most of the time
July 28, 1999	2877	MLS put in 'standby' to conserve lifetime for overlap with EOS Aura
Feb 2–12, 2000	3066–3076	MLS turned on for limited Arctic observations
Mar 27–30, 2000	3120–3123	MLS turned on for limited Arctic observations
Aug 18–25, 2001	3629–3636	MLS turned on for limited northern hemisphere observations and ODIN validation campaign
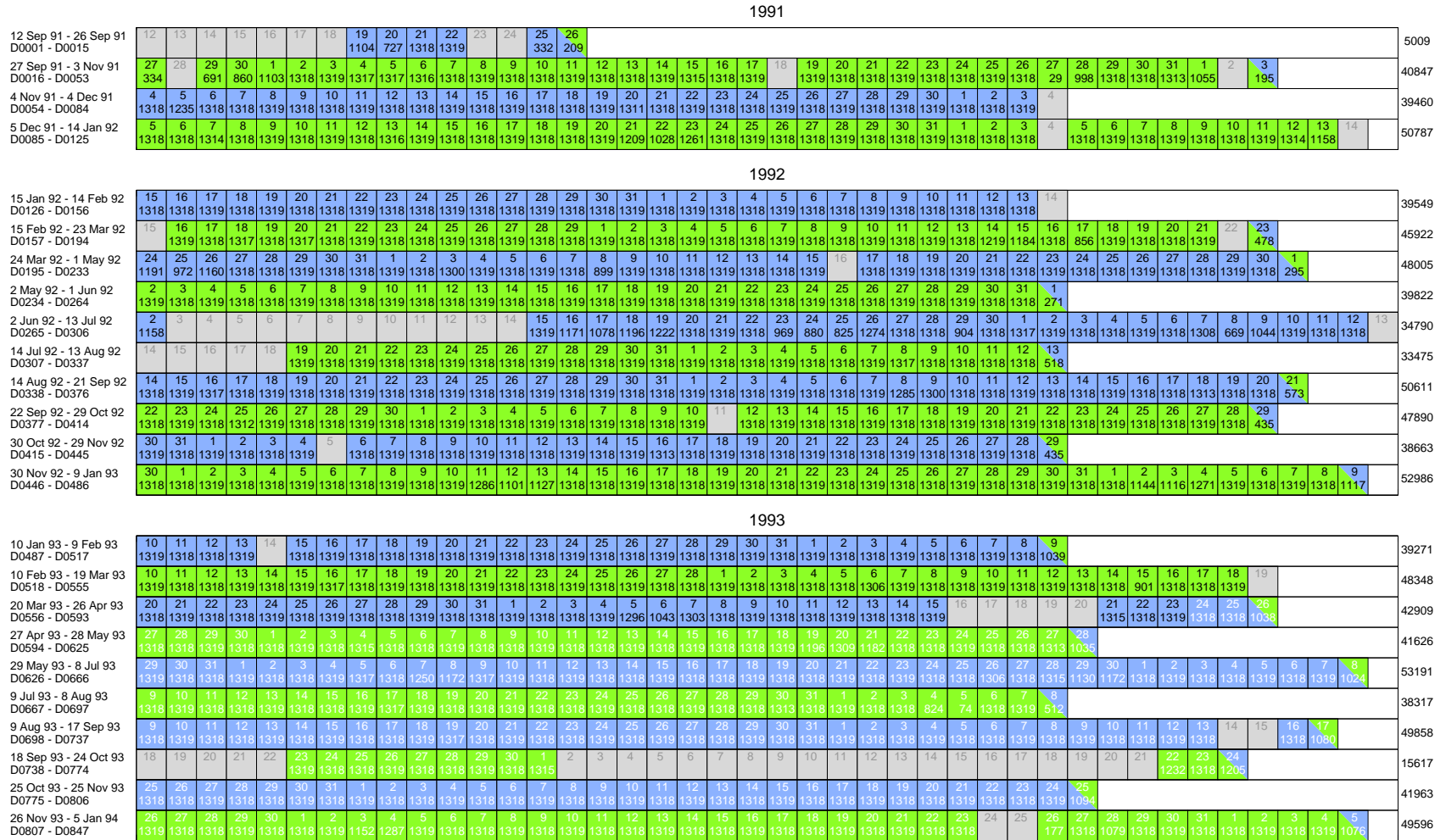
Figure S25. Calendars showing UARS MLS measurement coverage from 1991 through 1999. Each panel represents one year of data. Days are arranged in UARS 'months', or yaw cycles, which typically comprise 35–40 days and span more than one calendar month. The range of calendar dates and UARS mission day numbers for each UARS 'month' are given on the left side of each row. North-looking days are indicated by green shading, south-looking days by blue shading, and yaw days by split shading. Days for which the instrument was turned off or for other reasons no good limb scans were obtained are shown in grey. The numbers are black for days when all three radiometers were active, white for days following the failure of the 183-GHz radiometer, and red for those days where only the 205-GHz radiometer was operating. The top number in each of the shaded boxes indicates the day of month. The bottom number in the colored boxes indicates the total number of good limb scans on that day, which ranges between 1 and 1319. The sum of the number of good limb scans over the entire UARS 'month' is given to the right of each row (with the maximum attainable for a typical UARS 'month' being about 50,000).

Figure S25. Continued.

Figure S25. Continued.

References

Brasseur, G., and S. Solmon, *Aeronomy of the Middle Atmosphere*, D. Reidel, 1986, second edition.

Brune, W. H., D. W. Toohey, S. A. Lloyd, and J. G. Anderson, The sunrise and sunset variation of ClO in the lower stratosphere, *Geophys. Res. Lett.*, *17*, 509–512, 1990.

de Boor, C., *A Practical Guide to Splines*, Spinger-Verlag, 1987, fourth edition.

Dudhia, A., and N. J. Livesey, Validation of the Improved Stratospheric and Mesospheric Sounder temperature measurements, *J. Geophys. Res.*, *101*, 9795–9809, 1996.

Feist, D. G., C. P. Aellig, N. Kämpfer, P. M. Solomon, J. W. Barrett, S. Zoonematkermani, P. Hartogh, C. Jarchow, and J. W. Waters, Validation of stratospheric ClO measurements from the Millimeter-wave Atmospheric Sounder (MAS), *J. Geophys. Res.*, *105*, 9053–9062, 2000.

Froidevaux, L., M. Allen, and Y. L. Yung, A critical analysis of ClO and O_3 in the mid-latitude stratosphere, *J. Geophys. Res.*, *90*, 12,999–13,029, 1985.

Froidevaux, L., J. W. Waters, W. G. Read, P. S. Connell, D. E. Kinneson, and J. M. Russell, III, Variations in the free chlorine content of the stratosphere (1991–1997): Anthropogenic, volcanic, and methane influences, *J. Geophys. Res.*, *105*, 4471–4481, 2000.

Froidevaux, L., et al., Validation of UARS Microwave Limb Sounder ozone measurements, *J. Geophys. Res.*, *101*, 10,017–10,060, 1996.

Gunson, M. R., et al., The Atmospheric Trace Molecule Spectroscopy (ATMOS) experiment: Deployment on the ATLAS Space Shuttle missions, *Geophys. Res. Lett.*, *23*, 2333–2336, 1996.

Harries, J. E., et al., Validation of measurements of water vapour from the halogen occulation experiment (HALOE), *J. Geophys. Res.*, *101*, 10,205–10,216, 1996.

Isaacson, E., and H. B. Keller, *Analysis of Numerical Methods*, Dover, 1994.

Jarnot, R. F., R. E. Cofield, J. W. Waters, and D. A. Flower, Calibration of the Microwave Limb Sounder on the Upper Atmosphere Research Satellite, *J. Geophys. Res.*, *101*, 9957–9982, 1996.

Khosravi, R., G. P. Brasseur, A. K. Smith, D. W. Rusch, J. W. Waters, and J. M. Russell, III, Significant reduction in the stratospheric ozone deficit using a three-dimensional model constrained with UARS data, *J. Geophys. Res.*, *103*, 16,203–16,219, 1998.

Ko, M. W. K., and N. D. Sze, Diurnal variation of ClO: Implications for the Stratospheric Chemistries of $ClONO_2$, HOCl, and HCl, *J. Geophys. Res.*, *89*, 11,619–11,632, 1984.

Liebe, H. J., P. W. Rosenkranz, and G. A. Hufford, Atmospheric 60-GHz oxygen spectrum: New laboratory measurements and line parameters, *J. Quant. Spectrosc. Radiat. Transfer*, *48*, 629–643, 1992.

Lipson, J. B., M. J. Elrod, T. W. Beiderhase, L. T. Molina, and M. J. Molina, Temperature dependence of the rate constant and branching ratio for the OH + ClO reaction, *J. Chem. Soc. Faraday Trans.*, *83*, 2665–2673, 1997.

Livesey, N. J., J. W. Waters, R. Khosravi, G. P. Brasseur, G. S. Tyndall, and W. G. Read, Stratospheric CH_3CN from the UARS Microwave Limb Sounder, *Geophys. Res. Lett.*, *28*, 779–782, 2001.

Massie, S. T., X. X. Tie, G. P. Brasseur, R. M. Bevilacqua, M. D. Fromm, and M. L. Santee, Chlorine activation during the early 1995–1996 Arctic winter, *J. Geophys. Res.*, *105*, 7111–7131, 2000.

Michelsen, H. A., et al., ATMOS version 3 water vapor measurements: Comparisons with observations from two lyman-alpha hygrometers, MkIV, HALOE, SAGE II, MAS and MLS, *JGR*, in press.

Nedoluha, G. E., et al., A comparative study of mesospheric water vapor measurements from the ground-based water vapor millimeter-wave spectrometer and space-based instruments, *J. Geophys. Res.*, *102*, 16,647–16,661, 1997.

Pickett, H. M., Effects of velocity averaging on the shapes of absorption lines, *J. Chem. Physics*, *73*, 6090–6094, 1980.

Pickett, H. M., R. L. Poynter, and E. A. Cohen, Submillimeter, millimeter and microwave spectral line catalog, *Tech. rep.*, Jet Propulsion Laboratory, 1992, 80-23, Rev. 3.

Pumphrey, H. C., Validation of a new prototype water vapor retrieval for the UARS Microwave Limb Sounder, *J. Geophys. Res.*, *104*, 9399–9412, 1999.

Pumphrey, H. C., and S. Bühler, Instrumental and spectral parameters: Their effect on and measurement by microwave limb sounding of the atmosphere., *J. Quant. Spectrosc. Radiat. Transfer*, *64*, 421–437, 2000.

Pumphrey, H. C., D. Rind, J. M. Russell, III, and J. E. Harries, A preliminary zonal mean climatology of water vapour in the stratosphere and mesosphere, *Adv. Space. Res.*, *21*, 1417–1420, 1998.

Pumphrey, H. C., H. L. Clark, and R. S. Harwood, Lower stratospheric water vapor as measured by UARS MLS, *Geophys. Res. Lett.*, *27*, 1691–1694, 2000.

Read, W. G., L. Froidevaux, and J. W. Waters, Microwave Limb Sounder measurements of stratospheric SO_2 from the Mt. Pinatubo volcano, *Geophys. Res. Lett.*, *20*, 1299–1302, 1993.

Read, W. G., J. W. Waters, D. A. Flower, L. Froidevaux, R. F. Jarnot, D. L. Hartman, R. S. Harwood, and R. B. Rood, Upper–tropospheric water vapor from UARS MLS, *Bull. Amer. Meteorl. Soc.*, *76*, 2381–2389, 1995.

Read, W. G., et al., UARS Microwave Limb Sounder upper tropospheric humidity measurement: Method and validation, *J. Geophys. Res.*, *106*, 32,207–32,258, 2001.

Ricaud, P., J. de la Noë, B. J. Connor, L. Froidevaux, J. W. Waters, R. S. Harwood, I. A. MacKenize, and G. E. Peckham, Diurnal variability of mesospheric ozone as measured by the UARS Microwave Limb Sounder instrument: Theoretical and ground-based validations, *J. Geophys. Res.*, *101*, 10,077–10,089, 1996.

Ricaud, P., M. P. Chipperfield, J. W. Waters, J. M. Russell, III, and A. E. Roche, Temporal evolution of chlorine monoxide in the middle stratosphere, *J. Geophys. Res.*, *105*, 4459–4469, 2000.

Rodgers, C. D., Retrieval of atmospheric temperature and composition from remote measurements of thermal radiation, *Rev. Geophys.*, *14*, 609–624, 1976.

Rodgers, C. D., Characterisation and error analysis of profiles retrieved from remote sounding measurements, *J. Geophys. Res.*, *95*, 5587–5595, 1990.

Rodgers, C. D., *Inverse methods for atmospheric science, theory and practice*, World Scientific, 2000.

Santee, M. L., G. L. Manney, N. J. Livesey, and J. W. Waters, UARS Microwave Limb Sounder observations of denitrification and ozone loss in the 2000 Arctic late winter, *Geophys. Res. Lett.*, *27*, 3213–3216, 2000.

Shippony, Z., and W. Read, A correction to a highly accurate Voigt function algorithm, *J. Quant. Spectrosc. Radiat. Transfer*, 2002, in press.

Shippony, Z., and W. G. Read, A highly accurate Voigt function algorithm, *J. Quant. Spectrosc. Radiat. Transfer*, *50*, 635–646, 1993.

Siskind, D. E., L. Froidevaux, J. M. Russell, III, and J. Lean, Implications of upper stratospheric trace constituents observed by HALOE for O_3 and ClO from 1992 to 1995, *Geophys. Res. Lett.*, *25*, 3513–3516, 1998.

Tscherning, C. C., ed., *The Geodesist's Handbook*, vol. 58, Bureau Central De L'Association Internatiale De Géodésie, 1984.

vanVleck, J. H., and V. F. Weisskopf, On the shape of collision-broadened lines, *Rev. Mod. Phys.*, *17*, 227–236, 1945.

Wang, H. J., D. M. Cunnold, L. Froidevaux, and J. M. Russell, III, A reference model for middle atmosphere ozone in 1992–1993, *J. Geophys. Res.*, *104*, 21,629–21643, 1999.

Waters, J. W., L. Froidevaux, W. G. Read, G. L. Manney, L. S. Elson, D. F. Flower, R. F. Jarnot, and R. S. Harwood, Stratospheric ClO and ozone from the Microwave Limb Sounder on the Upper Atmosphere Research Satellite, *Nature*, *362*, 597–602, 1993.

Waters, J. W., et al., Validation of UARS Microwave Limb Sounder ClO measurements, *J. Geophys. Res.*, *101*, 10,091–10,127, 1996.

Waters, J. W., et al., The UARS and EOS Microwave Limb Sounder (MLS) experiments, *J. Atmos. Sci.*, *56*, 194–217, 1999.

Wu, D. L., and J. W. Waters, Gravity-wave-scale temperature fluctuations seen by the UARS MLS, *Geophys. Res. Lett.*, *23*, 3289–3202, 1996.

Jet Propulsion Laboratory, MS 183–701, 4800 Oak Grove Drive, Pasadena, CA 91109–8099